







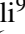

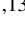
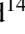


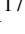




# Gas, dust, and the CO-to-molecular gas conversion factor in low-metallicity starbursts<sup>★</sup>

L. K. Hunt<sup>1</sup>, F. Belfiore<sup>1</sup>, F. Lelli<sup>1</sup>, B. T. Draine<sup>2</sup>, A. Marasco<sup>3,1</sup>, S. García-Burillo<sup>4</sup>, G. Venturi<sup>5,1</sup>, F. Combes<sup>6</sup>, A. Weiß<sup>7</sup>, C. Henkel<sup>7,8</sup>, K. M. Menten<sup>7</sup>, F. Annibali<sup>9</sup>, V. Casasola<sup>10</sup>, M. Cignoni<sup>11,12,13</sup>, A. McLeod<sup>14,15</sup>, M. Tosi<sup>9</sup>, M. Beltrán<sup>1</sup>, A. Concas<sup>16</sup>, G. Cresci<sup>1</sup>, M. Ginolfi<sup>17</sup>, N. Kumari<sup>18</sup>, and F. Mannucci<sup>1</sup>

<sup>1</sup> INAF – Osservatorio Astrofisico di Arcetri, Largo E. Fermi 5, 50125 Firenze, Italy  
e-mail: leslie.hunt@inaf.it

<sup>2</sup> Princeton University Observatory, Peyton Hall, Princeton, NJ 08544-1001, USA

<sup>3</sup> INAF – Osservatorio Astronomico di Padova, Vicolo dell’Osservatorio 5, 35122 Padova, Italy

<sup>4</sup> Observatorio Astronómico Nacional (OAN)-Observatorio de Madrid, Alfonso XII 3, 28014 Madrid, Spain

<sup>5</sup> Instituto de Astrofísica, Facultad de Física, Pontificia Universidad Católica de Chile, Casilla 306, Santiago 22, Chile

<sup>6</sup> Observatoire de Paris, LERMA, Collège de France, CNRS, PSL, Sorbonne University, 75014 Paris, France

<sup>7</sup> Max-Planck-Institut für Radioastronomie, Auf dem Hügel 69, 53121 Bonn, Germany

<sup>8</sup> Astronomy Department, King Abdulaziz University, PO Box 80203, Jeddah, Saudia Arabia

<sup>9</sup> INAF – Osservatorio di Astrofisica e Scienza dello Spazio, Via Piero Gobetti 93/3, 40129 Bologna, Italy

<sup>10</sup> INAF – Istituto di Radioastronomia, Via Piero Gobetti 93/3, 40129 Bologna, Italy

<sup>11</sup> Department of Physics – University of Pisa, Largo B. Pontecorvo 3, 56127 Pisa, Italy

<sup>12</sup> INFN – Istituto Nazionale di Fisica Nucleare, Largo B. Pontecorvo 3, 56127 Pisa, Italy

<sup>13</sup> INAF – Osservatorio Astronomico di Capodimonte, Via Moiariello 16, 80131 Napoli, Italy

<sup>14</sup> Centre for Extragalactic Astronomy, Department of Physics, Durham University, South Road, Durham DH1 3LE, UK

<sup>15</sup> Institute for Computational Cosmology, Department of Physics, University of Durham, South Road, Durham DH1 3LE, UK

<sup>16</sup> European Southern Observatory, Karl-Schwarzschild-Strasse 2, 85748 Garching bei München, Germany

<sup>17</sup> Dipartimento di Astronomia e Scienza dello Spazio, Università degli Studi di Firenze, Largo E. Fermi 2, 50125 Firenze, Italy

<sup>18</sup> AURA for the European Space Agency, Space Telescope Science Institute, 3700 San Martin Drive, Baltimore, MD 21218, USA

Received 27 December 2022 / Accepted 10 May 2023

## ABSTRACT

The factor relating CO emission to molecular hydrogen column density,  $X_{\text{CO}}$ , is still subject to uncertainty, in particular at low metallicity. In this paper, to quantify  $X_{\text{CO}}$  at two different spatial resolutions, we exploited a dust-based method together with ALMA 12-m and ACA data and HI maps of three nearby metal-poor starbursts, NGC 625, NGC 1705, and NGC 5253. Dust opacity at 250 pc resolution was derived based on dust temperatures estimated by fitting two-temperature modified blackbodies to *Herschel* PACS data. By using the HI maps, we were then able to estimate dust-to-gas ratios in the regions dominated by atomic gas, and, throughout the galaxy, to infer total gas column densities and  $\text{H}_2$  column densities as the difference with HI. Finally, from the ACA CO(1–0) maps, we derived  $X_{\text{CO}}$ . We used a similar technique with 40 pc ALMA 12-m data for the three galaxies, but instead derived dust attenuation at 40 pc resolution from reddening maps based on VLT/MUSE data. At 250 pc resolution, we find  $X_{\text{CO}} \sim 10^{22}–10^{23} \text{ cm}^{-2}/\text{K km s}^{-1}$ , 5–1000 times the Milky Way value, with much larger values than would be expected from a simple metallicity dependence. Instead, at 40 pc resolution,  $X_{\text{CO}}$  again shows large variation, but is roughly consistent with a power-law metallicity dependence, given the  $Z \sim 1/3 Z_{\odot}$  metal abundances of our targets. The large scatter in both estimations could imply additional parameter dependence, which we have investigated by comparing  $X_{\text{CO}}$  with the observed velocity-integrated brightness temperatures,  $I_{\text{CO}}$ , as predicted by recent simulations. Indeed, larger  $X_{\text{CO}}$  is significantly correlated with smaller  $I_{\text{CO}}$ , but with slightly different slopes and normalizations than predicted by theory. Such behavior can be attributed to the increasing fraction of CO-faint (or dark)  $\text{H}_2$  gas with lower spatial resolution (larger beams). This confirms the idea the  $X_{\text{CO}}$  is multivariate, depending not only on metallicity but also on the CO brightness temperature and beam size. Future work is needed to consolidate these empirical results by sampling galaxies with different metal abundances observed at varying spatial resolutions.

**Key words.** galaxies: starburst – galaxies: dwarf – galaxies: star formation – ISM: molecules – dust, extinction – galaxies: ISM

## 1. Introduction

From early cosmic times, molecular clouds are the cradles of star formation. However, molecular gas,  $\text{H}_2$ , is not easily traced

<sup>★</sup> This paper makes use of the following ALMA data: ADS/JAO.ALMA#2018.1.00219.S. ALMA is a partnership of ESO (representing its member states), NSF (USA), and NINS (Japan), together with NRC (Canada), MOST and ASIAA (Taiwan), and KASI (Republic of Korea), in cooperation with the Republic of Chile. The Joint ALMA Observatory is operated by ESO, AUI/NRAO, and NAOJ.

observationally. The rotational levels of  $\text{H}_2$  are widely separated, with negligible thermal excitation in cold clouds. In addition,  $\text{H}_2$  is a homonuclear diatomic molecule with no permanent dipole moment so that there are no rovibrational electric dipole transitions.

Luckily, molecular gas is not pure  $\text{H}_2$ , but also contains heavy trace elements. The abundances of oxygen and carbon in the interstellar medium (ISM) enable the formation of carbon monoxide (CO) within dense, cold, molecular clouds. Due to its low excitation energy in the ground-state rotational transition

( $h\nu/k_B \approx 5.5$  K) and its low critical density ( $\sim 1400$  cm $^{-3}$ , for a kinetic temperature  $T = 25$  K), CO emission can be easily excited even in cold molecular clouds<sup>1</sup>. Thus, the lowest-order CO transition  $J = 1 \rightarrow 0$  at 2.6 mm, which is fortunately located within a fairly transparent atmospheric window, has become a common tracer of H<sub>2</sub> in the Milky Way and external galaxies.

Nevertheless, CO has its own problems. Under typical ISM conditions, CO emission is optically thick, so that even when its abundance relative to H<sub>2</sub> is known, CO cannot be used to directly trace the molecular column density or mass along the line of sight. Thus, it is standard to connect the column (or mass) density of molecular gas  $N_{\text{H}_2}$  to the observed <sup>12</sup>CO(1–0) velocity-integrated brightness temperature,  $I_{\text{CO}}$ , via a CO-to-H<sub>2</sub> conversion factor,  $X_{\text{CO}}$ :

$$N_{\text{H}_2} = X_{\text{CO}} I_{\text{CO}}, \quad (1)$$

where the H<sub>2</sub> column density  $N_{\text{H}_2}$  is in units of cm $^{-2}$ , and  $I_{\text{CO}}$  is in units of K km s $^{-1}$ . The existence of a nearly constant  $X_{\text{CO}}$  at solar-like metallicities where H<sub>2</sub> and CO coexist to a large extent relies on the assumption that the optically thick CO emission comes from virialized clouds that do not overlap. Thus,  $X_{\text{CO}}$  is essentially an empirical shortcut to count clouds along the line of sight.

Although the conversion factor  $X_{\text{CO}}$  relating CO emission to H<sub>2</sub> mass  $M_{\text{H}_2}$  is relatively constant across the Galaxy (e.g., Sanders et al. 1984; Bolatto et al. 2013), at low metallicity and in starburst galaxies, its value is still uncertain. Inferring  $X_{\text{CO}}$  in metal-poor environments has been the subject of an enormous effort, both observational and theoretical (see Bolatto et al. 2013, for an extensive review). The problem lies in the complexity of the relation between CO emission and H<sub>2</sub>. Simulations and observational work have suggested that the amount of CO and its emission depends primarily on shielding, that is the protection of CO molecules from dissociating far-ultraviolet (FUV) radiation. Self-shielding of H<sub>2</sub> is highly efficient, meaning that the photodissociation rate of H<sub>2</sub> is typically very small wherever there is a significant amount of H<sub>2</sub>. On the other hand, self-shielding of CO and cross-shielding of CO by H<sub>2</sub> are inefficient processes (e.g., Gong et al. 2018). Consequently, CO needs additional protection by dust.

Photodissociation of CO tends to erode the CO-emitting regions of molecular clouds, even at solar metallicity. At sub-solar abundances, stars are hotter and have higher hard photon fluxes, enhancing the effect; thus the regions where H<sub>2</sub> resides are much larger than those where CO and H<sub>2</sub> coexist (e.g., van Dishoeck & Black 1988). Consequently, there are extended regions of so-called “CO-faint” (or dark) gas in which the dominant forms of carbon are ionized (C<sup>+</sup>) or neutral carbon (e.g., Wolfire et al. 2010). The CO-emitting regions in low-metallicity environments are expected to be much smaller (a few parsecs) than they would be in more typical, metal-rich, conditions (e.g., Bolatto et al. 1999, 2013). Indeed, the small size of CO-emitting clouds at low metallicity has been verified observationally in the Magellanic Clouds (e.g., Pak et al. 1998; Indebetouw et al. 2013; Tokuda et al. 2021), and in nearby dwarf galaxies (e.g., Rubio et al. 2015; Schrubba et al. 2017; Shi et al. 2020).

Early attempts at estimating  $X_{\text{CO}}$  theoretically relied on models of photodissociation regions which are able to resolve the thermal and chemical structure within an individual cloud (e.g., Wolfire et al. 1993; Bell et al. 2006). Later cloud models (e.g., Glover & Mac Low 2011; Shetty et al. 2011; Glover & Clark

2016), based on hydrodynamical simulations with more complex geometries and density structure, confirmed that  $X_{\text{CO}}$  varies with visual extinction  $A_V$ , or depth within the cloud. In particular, there was evidence for an extinction threshold above which clouds become CO bright (see also Bell et al. 2006). Metallicity plays a fundamental role because lower dust abundance provides less dust shielding against CO photodissociation, resulting in more extended regions of CO-faint gas. Cosmic-ray ionization is also emerging as an important parameter (e.g., Bisbas et al. 2021).

Global models of  $X_{\text{CO}}$  in galaxies using hydrodynamical simulations (e.g., Feldmann et al. 2012; Narayanan et al. 2012) suggest that  $X_{\text{CO}}$  depends on metallicity, dust extinction, and H<sub>2</sub> column density  $N_{\text{H}_2}$ ; in addition, there may be a dependence on observational spatial scale (see also Rubio et al. 1993) and velocity-integrated CO brightness temperature ( $T_B$ ),  $I_{\text{CO}}$ . These two latter trends reflect the fact that  $X_{\text{CO}}$  tends to be lower when estimated from regions with higher CO surface brightness; thus from an observational perspective, smaller beams generally give lower  $X_{\text{CO}}$ . In fact, CO observations with beam sizes of a few parsecs that resolve the central regions containing CO in low-metallicity molecular clouds tend to result in  $X_{\text{CO}}$  values that are roughly consistent with  $X_{\text{CO}}$  for the Milky Way (e.g., Bolatto et al. 2008).

The main problem with these global models for  $X_{\text{CO}}$  is the determination of the physical conditions and line-emission properties on subgrid scales. More recent models overcome this limitation through a better match of large-scale simulations and the physics and chemistry of small-scale resolved cloud structure. In the solar metallicity models of Gong et al. (2017, 2018, 2020), the average  $X_{\text{CO}}$  increases by a factor of  $\sim 2$  as the observational beam size grows from 1 to 100 pc. Moreover, the CO-dark H<sub>2</sub> fraction ranges from  $\sim 30$ – $80\%$ , and is anticorrelated with visual extinction. With models over a range of metallicities, Hu et al. (2022) find that the parsec-scale  $X_{\text{CO}}$  is roughly the Galactic value, independently of metallicity once dust shielding becomes effective. Hu et al. (2022) also find that CO emission becomes more optically thin at lower metallicity (see Hunt et al. 2017, for a tentative observational verification). The Hu et al. (2022) simulations also show that although most CO emission originates from dense gas with low  $X_{\text{CO}}$ , most of the cloud area is filled by diffuse gas with high  $X_{\text{CO}}$ . This leads to an anticorrelation of  $X_{\text{CO}}$  and  $I_{\text{CO}}$ , also implying that  $X_{\text{CO}}$  is leveraged by beam averaging, and tends to be biased toward the highest density regions of the molecular gas.

Here we attempt to test theoretical predictions of  $X_{\text{CO}}$  at low metallicity by observationally quantifying trends of  $X_{\text{CO}}$  with dust content and spatial resolution. Using CO maps of three iconic low-metallicity dwarf galaxies observed with the ALMA 12-m and compact (ACA, 7-m) arrays, at  $\sim 40$  pc and  $\sim 250$  pc resolutions, respectively, we first estimate dust content at  $\sim 250$  pc resolution. To do this, we calculate the dust opacity at  $160 \mu\text{m}$   $\tau_{160}$  from *Herschel* observations, and compare it with HI and CO maps at the same resolution. Then, we infer dust content at  $\sim 40$  pc resolution from VLT/MUSE maps of  $E(B - V)$  and compare it with the higher resolution CO maps. Finally, we compute  $X_{\text{CO}}$  at both resolutions, and compare the measured values with theoretical predictions. Section 2 describes the targets, and Sect. 3 the ALMA observations and our ancillary data. The determination of dust optical depth, gas content, and inference of  $X_{\text{CO}}$  on  $\sim 250$  pc scales is given in Sect. 4, while Sect. 5 reports an analogous assessment for  $X_{\text{CO}}$  at  $\sim 40$  pc resolution. The two sets of results are compared in Sect. 6, and Sect. 7 provides a brief discussion and our conclusions.

<sup>1</sup> This assumes an optically thin line; if optically thick, as is common for CO, the effective critical density would be even lower.

**Table 1.** Parameters for observed galaxies.

Name	Optical center (J2000) <sup>(a)</sup>		Redshift <sup>(a)</sup>	Distance (Mpc)	Distance method	$\log(M_*/M_\odot)$ <sup>(b)</sup>	$\log(\text{SFR}/M_\odot \text{ yr}^{-1})$ <sup>(b)</sup>	12+log(O/H) (direct $T_e$ method)
	RA	Dec						
NGC 625	01:35:04.63	-41:26:10.3	0.00132	3.90 <sup>(c)</sup>	TRGB <sup>(e)</sup>	8.58 ± 0.19	-1.22 ± 0.14	8.08 <sup>(f)</sup>
NGC 1705	04:54:13.50	-53:21:39.8	0.00211	5.22 <sup>(d)</sup>	TRGB <sup>(e)</sup>	8.08 ± 0.24	-1.35 ± 0.09	8.21 <sup>(f)</sup>
NGC 5253	13:39:55.96	-31:38:24.4	0.00136	3.31 <sup>(d)</sup>	TRGB <sup>(e)</sup>	8.59 ± 0.24	-0.31 ± 0.15	8.18 <sup>(g)</sup>

**Notes.** <sup>(a)</sup>Taken from NED; <sup>(b)</sup>Stellar masses and star-formation rates (SFRs) taken from Marasco et al. (2023) reported to the distances used here; <sup>(c)</sup>Lelli et al. (2014a); <sup>(d)</sup>Sabbi et al. (2018); <sup>(e)</sup>Tip of the Red Giant Branch; <sup>(f)</sup>Berg et al. (2012); <sup>(g)</sup>López-Sánchez et al. (2012). For NGC 5253, we have adopted O/H for HII-region A since it is closer to the brightest SSC, and more consistent with the previous determination by Kobulnicky et al. (1997) of 12+log(O/H) = 8.16.

## 2. The targets

For our ALMA study, we selected three nearby ( $\sim 3\text{--}5$  Mpc) metal-poor ( $Z/Z_\odot \sim 0.3$ ) dwarf starbursts having (a) HI observations necessary to quantify their total gas content (Lelli et al. 2014a); (b) *Hubble* Space Telescope (HST) color-magnitude diagrams (CMDs) to constrain their star-formation histories (SFHs) and “burstiness” (Cannon et al. 2003; Tosi et al. 2001; Annibali et al. 2009; McQuinn et al. 2010; Cignoni et al. 2018, 2019); (c) archival MUSE data, to infer high-resolution extinction maps; and (d) archival *Herschel* data, to infer color temperatures for dust opacity maps. These are the only southern galaxies in the parent sample of Lelli et al. (2014a) and enable the start of a statistical approach; their properties are given in Table 1.

– NGC 625 hosts a massive starburst with several luminous HII regions and Wolf-Rayet (W–R) spectral features (Skillman et al. 2003a,b). The current starburst is relatively long-lived ( $\geq 50$  Myr Cannon et al. 2003; McQuinn et al. 2010), and the extended episode of star formation, possibly caused by an interaction or merger (Côté et al. 2000), has apparently disrupted the HI disk (Cannon et al. 2004; Lelli et al. 2014a), and caused an outflow detected in UV absorption lines (Cannon et al. 2005).

– NGC 1705 had more recent starburst episodes than NGC 625, with the older of two bursts of star formation having occurred  $\sim 10\text{--}15$  Myr ago, and the younger one much more recently,  $\sim 3$  Myr ago (Annibali et al. 2009; Cignoni et al. 2018). NGC 1705 is rich in star clusters (Billett et al. 2002), with the most massive one being a Super Star Cluster (SSC; O’Connell & Gallagher 1994; Vázquez et al. 2004; Martins et al. 2012), that has roughly the  $\sim 15$  Myr age of the oldest starburst event. There is evidence for a low-velocity outflow seen through UV absorption (Heckman et al. 2001), but, unlike in NGC 625, the HI is configured in a regularly rotating disk (Elson et al. 2013; Lelli et al. 2014a). With *Spitzer* observations of NGC 1705, Cannon et al. (2006) find that the far-infrared dust morphology differs dramatically from the optical, with two dust clouds  $\sim 250$  pc approximately east and west of the central SSC, and apparently unrelated to it. These two dust clouds also show  $8\ \mu\text{m}$  emission, and the central SSC is coincident with an  $8\ \mu\text{m}$  peak.

– NGC 5253 harbors an extremely young starburst with many massive star clusters (e.g., Calzetti et al. 1997; Cresci et al. 2005), with the majority of them in the central regions having ages of  $\sim 1\text{--}10$  Myr (e.g., Calzetti et al. 2015). NGC 5253 is overall more active than NGC 1705. Nevertheless, its SFH shows little evidence of a burst over the last  $10\text{--}20$  Myr, but this could result from the extreme crowding and incompleteness of the central region where most of the current SF is concentrated (Cignoni et al. 2019). NGC 5253’s CMD suggests that star-formation activity has been occurring for  $\geq 450$  Myr, similar to the dynamical time of the galaxy (McQuinn et al. 2010). There

is also a substantial population of W–R stars (Schaerer et al. 1997; Westmoquette et al. 2013), consistent with the young age of the central clusters. The most massive cluster lies within a radio nebula (e.g., Turner et al. 2000), and is enshrouded by a dust cloud with  $A_V \sim 50$  mag (e.g., Calzetti et al. 2015). The HI in NGC 5253 is highly perturbed (e.g., Kobulnicky & Skillman 2008; López-Sánchez et al. 2012; Lelli et al. 2014a), with infalling neutral gas that is apparently triggering the powerful current starburst (e.g., López-Sánchez et al. 2012; Turner et al. 2015). In fact, the HI kinematics is consistent with a disk-like structure dominated by a radial inflow motion of  $25\ \text{km s}^{-1}$  (Lelli et al. 2014a).

Although our study does not depend on specific metallicities, relative trends could be important, and affected by abundance gradients. Metallicity gradients in late-type dwarf irregulars or blue compact dwarfs tend to be generally negligible ( $\leq 0.1$  dex, e.g., Croxall et al. 2009), less severe than those in more massive spirals (e.g., Pilyugin et al. 2015). Resolved abundance investigations of our targets (e.g., Westmoquette et al. 2013; Annibali et al. 2015; Monreal-Ibero et al. 2017) show this to be the case; there is no evidence for strong metallicity gradients in any of the dwarf starburst targets, although some of the O/H estimates in the literature may differ from the ones adopted here (e.g., Annibali et al. 2015).

## 3. The data

To perform our analysis, we have combined ALMA observations with three sets of ancillary publicly-available data as described below.

### 3.1. ALMA observations

We observed the  $^{12}\text{CO}(1\text{--}0)$  line and tried to detect the 3 mm continuum emission in the three targets, NGC 625, NGC 1705, and NGC 5253 with the ALMA 12-m and the ACA 7-m arrays during Cycle 6 using the Band 3 receivers (project-ID: #2018.1.00219.S; PI: Hunt). Other transitions including CN and  $\text{SO}_2$  were placed in different sidebands, and their analysis will be presented in future work. To cover the entire emitting regions of the galaxies, we adopted 3-point mosaics with the ALMA 12-m array and a single pointing with ACA, obtaining a field-of-view of  $\sim 40''$ .

Data calibration and imaging for the 12-m and ACA data were done using the Common Astronomy Software Applications<sup>2</sup> (CASA, McMullin et al. 2007) version 6.2.1.7. The visibility data were calibrated in the standard way. We retained the native velocity resolution of 976.6 kHz channels, corresponding to  $\sim 2.5\ \text{km s}^{-1}$ . Imaging was performed with the `tclean` task

<sup>2</sup> <http://casa.nrao.edu/>

**Table 2.** Observational CO parameters.

Name	$V_{\text{sys}}^{(a)}$ ( $\text{km s}^{-1}$ )	FWZI $^{(b)}$ ( $\text{km s}^{-1}$ )	Imaged area	12 m beam	12 m rms ( $\text{mJy beam}^{-1}$ )	12 m total $^{(c)}$ ( $\text{Jy km s}^{-1}$ )	12 m total $^{(d)}$ ( $\text{Jy km s}^{-1}$ )	12 m total $^{(e)}$ ( $10^5 \text{ K km s}^{-1} \text{ pc}^2$ )
(1)	(2)	(3)	(4)	(5)	(6)	(7)	(8)	(9)
NGC 625	395.50	[-45, -5]	46" × 30"	2"08 × 1"49 (85.7°) 39 pc × 28 pc	1.4	15.2 ± 1.5	14.19 ± 1.4	5.64
NGC 1705	631.93	[-50, -5; 80, 102]	40" × 30"	2"49 × 1"82 (-83.9°) 63 pc × 46 pc	1.2	0.95 ± 0.05	0.86 ± 0.05	0.63
NGC 5253	406.56	[-50, 40]	50" × 30"	2"68 × 2"41 (85.3°) 43 pc × 39 pc	1.3	12.5 ± 0.04	12.1 ± 0.1	3.35
				7 m beam	7 m rms ( $\text{mJy beam}^{-1}$ )	7 m total $^{(c)}$ ( $\text{Jy km s}^{-1}$ )	7 m total $^{(d)}$ ( $\text{Jy km s}^{-1}$ )	7 m total $^{(e)}$ ( $10^5 \text{ K km s}^{-1} \text{ pc}^2$ )
NGC 625				12"1 × 7"8 (89.0°) 229 pc × 147 pc	6.4	14.85 ± 1.5	14.7 ± 1.5	5.52
NGC 1705				12"4 × 9"1 (89.9°) 314 pc × 230 pc	7.0	0.55 ± 0.05	0.44 ± 0.05	0.37
NGC 5253				13"0 × 7"9 (89.7°) 209 pc × 127 pc	6.4	14.1 ± 1.3	13.8 ± 1.2	3.77

**Notes.**  $^{(a)}$ Radio convention systemic velocity from observed sky frequency;  $^{(b)}$ full-width zero intensity (FWZI) as shown in Fig. 1;  $^{(c)}$ flux in all available pixels in the velocity-weighted line-intensity (zero moment) maps;  $^{(d)}$ flux with  $S/N \geq 3$  in zero moment maps;  $^{(e)}$ CO line luminosity.

using a Hogbom deconvolver and Briggs weighting with a robust parameter of 0.5.

For ACA, we set the pixel size of the cubes to 2"0, corresponding to  $\sim 1/6$  of the synthesized beams. The ACA cubes have typical rms noise levels  $\sigma$  of (6.4, 7.0, 6.4)  $\text{mJy beam}^{-1}$  for (NGC 625, NGC 1705, NGC 5253), respectively in velocity channels of  $2.5 \text{ km s}^{-1}$ . The pixel size of the ALMA 12-m cubes was set to 0"18,  $\sim 1/11$  of the synthesized beams. The final 12-m CO cubes have typical rms  $\sigma$  of (1.4, 1.2, 1.3)  $\text{mJy beam}^{-1}$  in velocity channels of  $2.5 \text{ km s}^{-1}$ . Table 2 gives details on the CO observations for each galaxy.

Examining the  $uv$  data showed that continuum emission is present only in NGC 5253; the continuum subtraction was performed by fitting and subtracting a first-order polynomial to line-free channels, in the  $uv$  as well as in the image planes, giving similar results. Ultimately, our final cube for NGC 5253 subtracts the continuum estimated from the image plane.

The 12-m and ACA CO data were analyzed separately, so that there are two data cubes for each galaxy. We derive total-intensity (moment-zero) maps using the task `Makemask` in `3DBarolo` (Di Teodoro & Fraternali 2015). This task sums the signal inside a Boolean mask, which is created by smoothing the cube in space and velocity and applying specific noise thresholds (see `3DBarolo` documentation for details). For this purpose, we use emission-line cubes without correction for primary beam attenuation, so the noise level is uniform and well defined across each channel map. The primary-beam correction is then applied directly to the moment-zero map. When using a Boolean mask to create a moment-zero map, the noise in the map varies from pixel to pixel because a different number of channels is summed up at each spatial position. We build a signal-to-noise (S/N) map using the relevant equation in the Appendix of Lelli et al. (2014b).

Total fluxes are estimated by summing the signal in the line-intensity (moment-zero) maps, or by summing the emission within a certain aperture in the data cubes (performed by `CASA/imview`). The two techniques give similar results. Figure 1 shows the ACA and 12-m spectra taken from this sum using polygonal apertures. Total fluxes for both the ACA and the 12-m array are given in Table 2. The ACA and 12-m fluxes are comparable, showing that we are not losing significant flux through interferometric filtering. For NGC 1705, the 12-m integrated flux is higher than for the ACA, by almost a factor of two,

suggesting that the CO emission is intrinsically compact and the ACA data suffer from low signal-to-noise.

### 3.2. Ancillary data

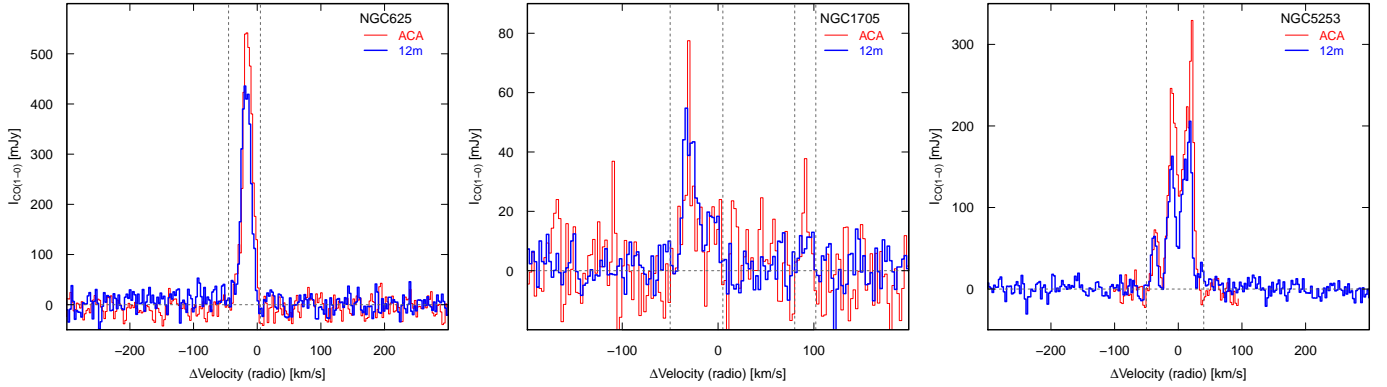
We have used ancillary data at different resolutions to estimate dust column density and compare it to our CO maps. The VLT/MUSE  $E(B - V)$  images are compared with the 12-m ALMA CO ( $\sim 40 \text{ pc}$ ), and the *Herschel*/PACS and HI with the ACA CO ( $\sim 250 \text{ pc}$ ).

#### 3.2.1. VLT/MUSE

Data from the MUSE optical integral field spectrograph at the ESO Very Large Telescope (VLT) obtained from the DWALIN (Dwarf galaxies Archival Local survey for Interstellar medium investigation) survey database (Marasco et al. 2023). Briefly, the DWALIN sample consists of 40 nearby galaxies with archival MUSE observations selected either from (a) the *Herschel* Dwarf Galaxy Survey (Madden et al. 2013), or (b) the Karachentsev et al. (2013) catalog, with distance  $D < 11 \text{ Mpc}$  and  $\log(M_{\text{star}}/M_{\odot}) < 9.0$ .

For NGC 1705, the original data were obtained from program 094.B-0745 (PI: García-Benito). The two available MUSE pointings were stitched together to form a mosaic. For NGC 5253, original data were taken from programs 094.B-0745 (PI: García-Benito) and 095.B-0321 (PI: Vanzi). In producing the final cube some exposures were discarded due to poor seeing. For NGC 625, we used data from 094.B-0745 (PI: García-Benito) and considered only 3 of the 4 exposures due to a guiding failure during the first exposure.

The MUSE data reduction was performed using the MUSE pipeline (Weilbacher et al. 2020) v2.8.1, with the ESO Recipe flexible execution workbench (Reflex; Freudling et al. 2013), which gives a graphical and automated way to execute with `EsoRex` the Common Pipeline Library (CPL) reduction recipes, within the Kepler workflow engine (Altintas et al. 2006). The absolute astrometry of the final mosaics is fixed to that of archival HST imaging. In the case of NGC 625 and NGC 5253,  $H\alpha$  emission is saturated in the regions of brightest line emission. These regions and the surrounding area were masked by hand.



**Fig. 1.** CO spectra of the target galaxies within an aperture containing the totality of CO emission regions plotted against velocity, where  $V_{\text{sys}}$  is given in Table 2. The full-width at zero intensity (FWZI) corresponds to the vertical dotted lines (see Table 2, Col. (2)). The 12-m spectra are shown in blue, and the ACA in red. In NGC 5253, these are both continuum-subtracted spectra. More details are given in the text.

Emission line maps were derived using the PHANGS data analysis pipeline<sup>3</sup> described in Emsellem et al. (2022). In short, the pipeline fits the stellar continuum using a set of E-MILES (Vazdekis et al. 2016) simple stellar population templates. Spectral fitting is carried out twice, first to derive the stellar kinematics, and a second time simultaneously with Gaussian templates for modeling the emission lines. Line maps are corrected for Milky Way foreground extinction.

Dust attenuation intrinsic to the galaxies is calculated using the Balmer decrement ( $H\alpha/H\beta$ ) and assuming Case B recombination, temperature  $T = 10^4$  K and density  $n_e = 10^2 \text{ cm}^{-3}$ , leading to  $L_{H\alpha}/L_{H\beta} = 2.86$ . We also assume the extinction law of O’Donnell (1994) with total-to-selective extinction  $R_V = 3.1$ , which is identical to the canonical Cardelli et al. (1989) parameterization. In the regions where  $H\alpha$  is saturated we have sufficient signal-to-noise to detect the hydrogen Paschen 10 (P10, at  $\lambda = 9017.5 \text{ \AA}$ ) line, which is then used in combination with  $H\beta$  to calculate the dust attenuation using the predicted ratio from Case B  $L_{P10}/L_{H\beta} = 0.0184$ . The CCD artifacts for the  $E(B - V)$  map of NGC 1705 do not impact our analysis. The global values of  $E(B - V)$  for our targets (Cignoni et al. 2019) are consistent with the spread of spatially resolved  $E(B - V)$  resulting from our calculations.

### 3.2.2. *Herschel* PACS

We acquired from the *Herschel* archive the raw scans taken with the Photodetector Array Camera and Spectrometer (PACS, Poglitsch et al. 2010) in the context of the *Herschel* Dwarf Galaxy Survey (Madden et al. 2013). The data available for our three targets at 70, 100, and 160  $\mu\text{m}$  have full widths at half maximum (FWHM) of  $5''.6$ ,  $6''.8$ , and  $11''.4$ , respectively. We reduced the raw scans using (the final) version 15.0.1 of the *Herschel* Interactive Processing Environment (HIPE; Ott et al. 2010) with the PACS\_CAL\_78\_0 photometric calibration, and adopting the scanam procedure to optimize extended emission. Sky subtraction was performed within the procedure but also subsequently checked to ensure roughly zero background. The reduced, calibrated images were generated with  $2''0$  pixels, and to be on the same resolution scale, were then convolved to the PACS 160  $\mu\text{m}$  FWHM using kernels from Aniano et al. (2011).

<sup>3</sup> <https://gitlab.com/francbelf/ifu-pipeline>

### 3.2.3. Atomic gas, HI

We reanalyze HI data from Lelli et al. (2014a) using HI cubes with the highest available angular resolution; beam sizes are ( $16''.9 \times 10''.6$ ,  $8''.5 \times 6''.6$ ,  $13''.6 \times 7''.5$ ) for (NGC 625, NGC 1705, NGC 5253), respectively. The HI data were obtained with the Very Large Array (VLA) for NGC 625 (Lelli et al. 2014a) and the Australia Telescope Compact Array (ATCA) for NGC 1705 (Elson et al. 2013) and NGC 5253 (López-Sánchez et al. 2012). We refer to those papers for details on observations and data reduction. Total-intensity (moment-zero) HI maps are derived using the same strategy as for CO maps (Sect. 3.1).

### 3.3. Image alignment and rebinning

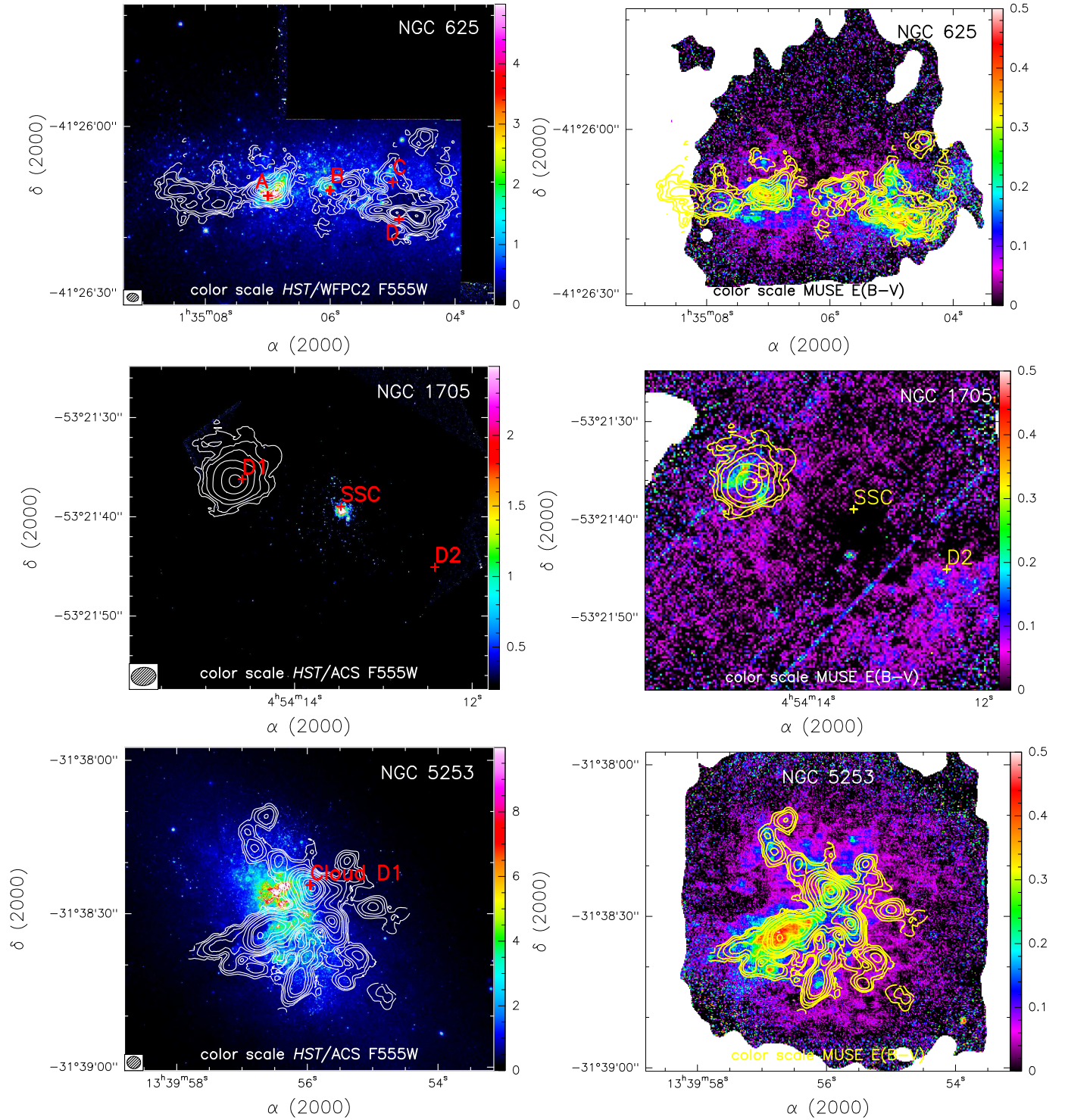
The ACA CO, HI, and (convolved) PACS images have been aligned to a common center and pixel size ( $2''$ ) using the routines within the GNU Astronomy Utilities (gnuastro<sup>4</sup>; Akhlaghi 2018). The 12-m and MUSE  $E(B - V)$  maps have been aligned with the same techniques, but instead with an intrinsic pixel size of  $0''.4$ . The alignment relies on the internal astrometric keywords, and thus implicitly assumes that the nominal astrometry is correct.

As mentioned above, the nominal MUSE astrometry was checked against HST and corrected as necessary. For NGC 625, there is a known discrepancy of the HST astrometry of the image used here (Cannon et al. 2003), and this was taken into account. For NGC 1705, a southward shift of  $2''.5$  was imposed on the nominal MUSE pipeline astrometry solution in order to align with HST and ALMA.

The rebinning to large pixels was performed within the *R* statistical package<sup>5</sup>. For the 12-m comparison of CO with  $E(B - V)$  we used resolution elements (pixels) of  $2''$  on a side, and for the ACA comparison with HI and PACS, pixels of ( $13''$ ,  $10''$ ,  $15''$ ) for (NGC 625, NGC 1705, and NGC 5253), respectively. The 12-m rebinning corresponds to  $\sim 40$  pc (see Table 2) and the ACA rebinning to  $\sim 250$  pc; the aim of the pixel sizes for ACA, HI, and PACS is to account approximately for the differences in distance of the targets.

<sup>4</sup> <https://www.gnu.org/software/gnuastro/>

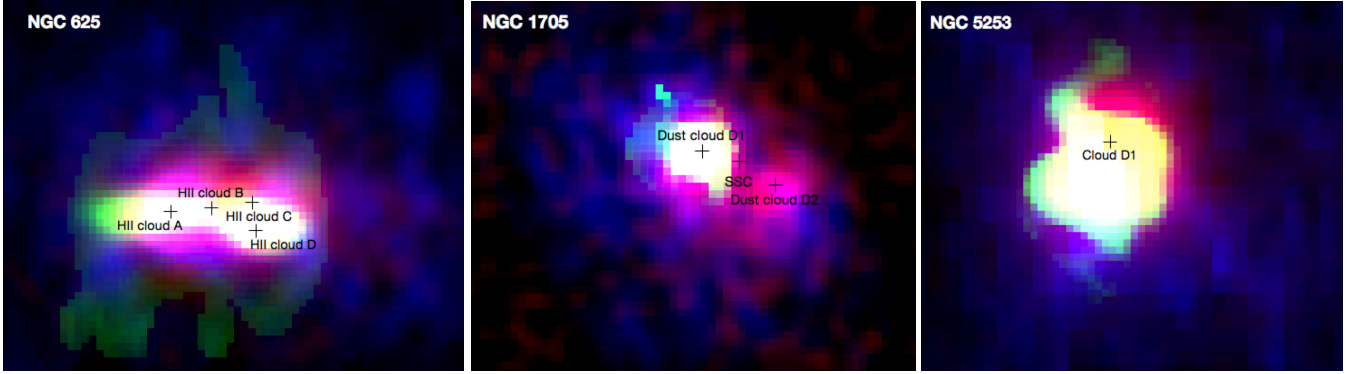
<sup>5</sup> For all statistical analysis, we rely on the *R* statistical package: R Core Team (2018), R: A language and environment for statistical computing, R Foundation for Statistical Computing, Vienna, Austria (<https://www.R-project.org/>).



**Fig. 2.** Contours of  $^{12}\text{CO}(1-0)$  (12-m) overlaid on HST  $F555W$  images (left panels), and MUSE  $E(B - V)$  maps (right). The  $^{12}\text{CO}(1-0)$  contour levels correspond to (0.01, 0.025, 0.05, 0.1, 0.2, 0.3, 0.4, 0.450, 0.750)  $\text{Jy km s}^{-1} \text{beam}^{-1}$  for NGC 625; (0.01, 0.025, 0.05, 0.1, 0.2, 0.3)  $\text{Jy km s}^{-1} \text{beam}^{-1}$  for NGC 1705; (0.01, 0.025, 0.05, 0.1, 0.15, 0.25, 0.4, 0.5, 0.75, 1.0, 1.5)  $\text{Jy km s}^{-1} \text{beam}^{-1}$  for NGC 5253. Also marked A–D in the left panels are the HII regions identified with radio continuum maps of NGC 625 by Cannon et al. (2004); the dust clouds and SSC in NGC 1705 identified from *Spitzer* observations (Cannon et al. 2006); and the unusual CO+dust cloud “D1” in NGC 5253 that coincides with the brightest, highly dust embedded SSC (Turner et al. 2017). The ALMA 12-m beam is shown in the lower-left corner of the left panels.

Figure 2 shows the results of the small spatial scale ( $\sim 40$  pc) alignments, where the 12-m CO zero-moment maps are overlaid on HST  $F555W$  images (left panel) and on the MUSE  $E(B - V)$  images (right). Also shown in Fig. 2 are specific features identified by previous work (e.g., Cannon et al. 2004, 2006;

Turner et al. 2017): HII regions (NGC 625) and dust clouds (NGC 1705, NGC 5253). Interestingly, in NGC 1705, PAH emission with *Spitzer*/IRS is only present in the eastern dust cloud D1 (Cannon et al. 2006) which is also the only location of CO emission. In all three galaxies, CO emission is not always coincident



**Fig. 3.** Color RGB images for NGC 625 (left panel), NGC 1705 (middle), and NGC 5253 (right) with *Herschel*/PACS-R as red, ACA  $^{12}\text{CO}(1-0)$  as green, and HI as blue; North is up, East is to the left. The image dimensions are  $130 \times 105 \text{ arcsec}^2$  for NGC 625, NGC 1705, and  $120 \times 105 \text{ arcsec}^2$  for NGC 5253. All observations have roughly spatial resolutions of  $\sim 250 \text{ pc}$  (see text for more details). The white color indicates where HI, CO, and dust are cospatial. As in Fig. 2, also indicated are the HII regions A–D of NGC 625 (Cannon et al. 2004); the dust clouds and SSC in NGC 1705 (Cannon et al. 2006); and the unusual CO+dust cloud “D1” in NGC 5253 that coincides with the brightest, highly dust embedded SSC (Turner et al. 2017).

with the stars traced by the HST images; in contrast, it almost perfectly coincides with  $E(B - V)$  from MUSE.

Figure 3 reports “false-color” RGB images at  $\sim 250 \text{ pc}$  resolution for the three target galaxies, using HI as blue, CO integrated intensity (zero-moment) maps as green, and PACS  $160 \mu\text{m}$  as red. As in Fig. 2, the salient features identified in previous work (Cannon et al. 2004, 2006; Turner et al. 2017) are also shown. The green “spur” to the east in NGC 625 shows that CO emission is present even without significant dust emission (traced by PACS); the diffuse HI emission is not well traced by this higher-resolution HI map (see Lelli et al. 2014a). In NGC 1705, the white colors of dust cloud D1 (Cannon et al. 2006) show that CO is cospatial with HI and dust, but, as also illustrated in Fig. 2, there is no CO in the second dust cloud D2, nor at the central SSC. On the other hand, the SSC embedded within cloud D1 in NGC 5253 (Turner et al. 2017), is cospatial with CO emission, as also shown at higher resolution in Fig. 2. In all three galaxies, HI is ubiquitous, more extended than the dust and the CO emission.

### 3.4. Comparison with previous CO flux measurements

Although NGC 1705 was not previously observed in CO, the two other targets have prior CO observations. NGC 625 was observed in  $^{12}\text{CO}(1-0)$  with the MOPRA 22-m single dish by Cormier et al. (2014) and with ALMA by Imara et al. (2020). The total CO velocity-integrated  $T_{\text{B}} I_{\text{CO}}$  given by Cormier et al. (2014) is  $4.3 \pm 0.6 \text{ K km s}^{-1}$ , or a  $\text{CO}(1-0)$  luminosity of  $1.1 \times 10^6 \text{ K km s}^{-1} \text{ pc}^2$ . With ALMA, in a  $\sim 1'31 \times 1'08$  beam, Imara et al. (2020) find  $I_{\text{CO}} = 3.0 \pm 0.2 \text{ K km s}^{-1}$ , that over a region of  $57'5 \times 20'$ , gives a luminosity of  $1.2 \times 10^6 \text{ K km s}^{-1} \text{ pc}^2$ . Since Cormier et al. (2014) and Imara et al. (2020) give total CO in units of velocity-integrated  $T_{\text{B}}$ , as averages over regions much larger than the beams, we compare our measurements as given in Table 2 with their luminosities;  $15.20 \text{ Jy km s}^{-1}$  corresponds to a luminosity of  $0.6 \times 10^6 \text{ K km s}^{-1} \text{ pc}^2$ , about half that measured by previous work. Since we find roughly the same velocity-integrated fluxes with the 12-m and ACA 7-m arrays, we would argue that the problem is not so much missing flux as possible differences in reduction and analysis procedures. The similarity of our integrated values with both arrays implies that this possible discrepancy will not significantly impact our results.

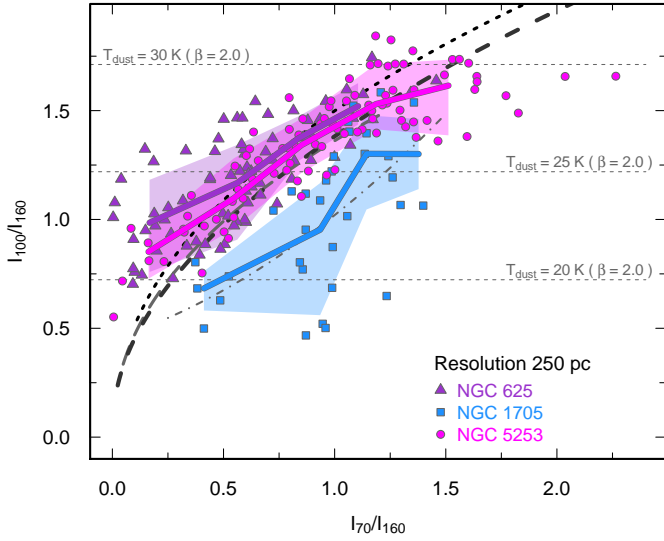
Wiklind & Henkel (1989) and Turner et al. (1997) have observed NGC 5253 with the 15 m Swedish-ESO Submillimeter Telescope (SEST,  $45''$  beam) and the Owens Valley Radio Observatory (OVRO), respectively. Wiklind & Henkel (1989) report a total velocity-integrated  $T_{\text{B}} I_{\text{CO}} = 1.3 \text{ K km s}^{-1}$ , with a velocity width of  $43 \text{ km s}^{-1}$ . With OVRO, using a  $14'9 \times 11'4$  beam, Turner et al. (1997) find a velocity-integrated flux of  $14.0 \text{ Jy km s}^{-1}$ , comparable to the flux recovered by our observations. NGC 5253 was also observed with ALMA in  $^{12}\text{CO}(2-1)$  by Miura et al. (2018), with the 12-m and 7-m arrays, and also with Total Power (TP). Within a box of  $90'' \times 84''$ , Miura et al. (2018) find  $96.6 \pm 0.2 \text{ Jy km s}^{-1}$  (TP), and within a region of  $22''$  radius  $92.6 \pm 0.1 \text{ Jy km s}^{-1}$  (combined TP+12m+7m). To compare their  $\text{CO}(2-1)$  observations with  $\text{CO}(1-0)$  from Wiklind & Henkel (1989), Miura et al. (2018) derive a TP velocity-integrated flux in  $\text{CO}(2-1)$  of  $42.3 \text{ Jy km s}^{-1}$ , centered on the Wiklind et al. SEST beam with a radius of  $22''$ . If CO is thermalized, as Miura et al. (2018) assume, this latter measurement would translate roughly into  $I_{\text{CO}} \approx 10.6 \text{ Jy km s}^{-1}$  for  $^{12}\text{CO}(1-0)$ , between 75% and 85% of our values in Table 2 over a similarly-sized area. Given the variation of the velocity-integrated fluxes found by Miura et al. (2018) in the different regions, our measurement is roughly consistent with previous work. In any case, as for NGC 625, the difference in our velocity-integrated CO flux with the 12-m and the 7-m arrays for NGC 5253 is not so large as to adversely affect our results for  $X_{\text{CO}}$ .

## 4. Large-scale dust opacity, gas content, and the $X_{\text{CO}}$ conversion factor

We trace the dust content along a line of sight at  $\sim 250 \text{ pc}$  resolution using the optical depth at  $160 \mu\text{m}$ ,  $\tau_{160}$  (e.g., Leroy et al. 2009; Bolatto et al. 2011). We then compare the distribution of  $\tau_{160}$  with the distributions of HI and ACA  $^{12}\text{CO}(1-0)$  at an angular resolution of  $\sim 250 \text{ pc}$ . Finally, we infer the  $\text{H}_2$  column density from the estimated dust-to-gas column density ratios, and derive the  $X_{\text{CO}}$  conversion factor.

### 4.1. Infrared dust opacity from *Herschel*/PACS

With the exception of extreme ultra-luminous infrared galaxies (e.g., Arp 220; Wilson et al. 2014), the assumption that dust



**Fig. 4.** PACS flux ratios  $I_{100}/I_{160}$  versus  $I_{70}/I_{160}$ . The PACS data have been rebinned to  $\sim 250$  pc resolution in order to match the HI and ACA CO maps. Heavy curves show the medians in  $I_{100}/I_{160}$  bins for each galaxy, and the shaded regions indicate  $1\sigma$  standard deviations. Also shown are the model MBB-T2 flux ratios with  $\gamma = 0.14$  (the median value for NGC 1705), indicated by the heavy black long-dashed curve. The IR ratios from two MBB models ( $\gamma = 0$ ) are illustrated as a long-dashed (gray) curve with  $\beta = 1$  (virtually indistinguishable from the MBB-T2 curve), and a short-dashed (black) curve for  $\beta = 2$ . The dot-dashed curve corresponds to the best fit polynomial for the SMC by Leroy et al. (2009). The horizontal lines illustrate the  $I_{100}/I_{160}$  ratios that would be expected for  $T_{\text{dust}} = 20$  K, 25 K, and 30 K. The line ratios for NGC 625 and NGC 5253 are fairly well approximated by MBBs or MBB-T2 fits, while the polynomial fit by Leroy et al. (2009) is a better approximation for NGC 1705. This fit is roughly equivalent to assuming that only half of the observed  $70\ \mu\text{m}$  emission comes from large, “classical” grains, with the other half originating from stochastic heating of small grains.

emission in galaxies is optically thin at  $160\ \mu\text{m}$  is well established (e.g., Misselt et al. 2001; Whelan et al. 2011). For an optically thin dust grain population with an equilibrium temperature,  $T_{\text{dust}}$ ,  $\tau_{160}$  is related to the measured  $160\ \mu\text{m}$  flux,  $I_{160}$ , by:

$$\tau_{160} = \frac{I_{160}}{B_{\nu}(T_{\text{dust}}, 160\ \mu\text{m})}, \quad (2)$$

where  $B_{\nu}$  corresponds to the intensity of a blackbody emitting at a temperature  $T_{\text{dust}}$  at wavelength  $\lambda$ . Thus, to compute  $\tau_{160}$ , we need to estimate the equilibrium dust temperature,  $T_{\text{dust}}$ .

To determine  $T_{\text{dust}}$ , the PACS 70, 100, and  $160\ \mu\text{m}$  data have been fit with two functions. One is an “MBB fit”, that is a single-temperature modified blackbody (MBB) with emissivity index  $\beta = 2.0$  having two fitted parameters:  $\tau_{160}$  and  $T_{\text{dust}}$ . The choice of  $\beta = 2$  is consistent with current estimates for the  $70$ – $160\ \mu\text{m}$  opacity of dust in the diffuse ISM in the solar neighborhood (Hensley & Draine 2021). The second is an “MBB-2T fit”, namely the sum of two MBBs with emissivity index  $\beta = 2.0$  with dust temperatures  $T_{\text{cool}}$  and  $T_{\text{warm}} = 1.5 \times T_{\text{cool}}$ . The two-temperature model is intended as a first approximation to the distribution of dust temperatures in a star-forming galaxy, where dust near newly-formed star clusters will be heated by more intense radiation. The choice of  $T_{\text{warm}}/T_{\text{cool}} = 1.5$  is somewhat arbitrary, but is motivated by the factor of  $\sim 2.3$  range of wavelengths ( $70\ \mu\text{m}$ – $160\ \mu\text{m}$ ) used in the fit. These fits have three fitted parameters:  $\tau_{160}$ ,  $T_{\text{cool}}$ , and  $\gamma$  defined as the fraction of the

dust emission due to the warmer component. For these fits, there are zero degrees of freedom since the fits are limited to the three PACS cameras because we want to preserve the  $250$  pc resolution (and the longer *Herschel*/SPIRE wavelengths give, at best, a resolution  $50\%$  worse).

The MBB-2T fitting function is given by:

$$I_{\nu} = \tau_{160} \left( \frac{2h\nu^3}{c^2} \right) \left( \frac{\nu}{\nu_0} \right) \left[ \frac{1 - \gamma}{e^{h\nu/kT_{\text{cool}}} - 1} + \frac{\gamma}{e^{h\nu/kT_{\text{warm}}} - 1} \right], \quad (3)$$

where  $\tau_{160}$  is the PACS  $160\ \mu\text{m}$  opacity,  $\nu_0$  corresponds to PACS  $160\ \mu\text{m}$ ,  $\gamma$  is the fraction of the dust emission due to the warmer component, and  $T_{\text{warm}}$  and  $T_{\text{cool}}$  are the warm and cool dust temperatures defined above. The MBB model is merely Eq. (3) with  $\gamma = 0$  and  $T_{\text{dust}} = T_{\text{cool}}$ . Since it is the cool dust with  $T = T_{\text{cool}}$  that defines  $\tau_{160}$ , the MBB-T2 model is better for our purposes. We know that there is temperature mixing along the line-of-sight, and thus almost certainly a component of warmer dust that would skew the determination of  $\tau_{160}$ . Hence, we also define an effective temperature:

$$T_{\text{dust}} = [(1 - \gamma) + \gamma(1.5)^6]^{1/6} T_{\text{cool}}. \quad (4)$$

The observed PACS flux ratios are shown in Fig. 4, together with individual MBB and MBB-T2 models. The comparison of IR ratios from two MBB models, with  $\beta = 1, 2$  and the MBB-T2 model with  $\gamma = 0.14$ , the median value for NGC 1705, shows that the two-temperature MBB-T2 model with  $\beta = 2$  mimics the MBB curve with lower emissivity,  $\beta = 1$ . This is a crude, although effective, example of temperature mixing being able to reproduce flat spectral emissivity with  $\beta \lesssim 1$  (e.g., Hunt et al. 2015), which however does not represent grain physical properties.

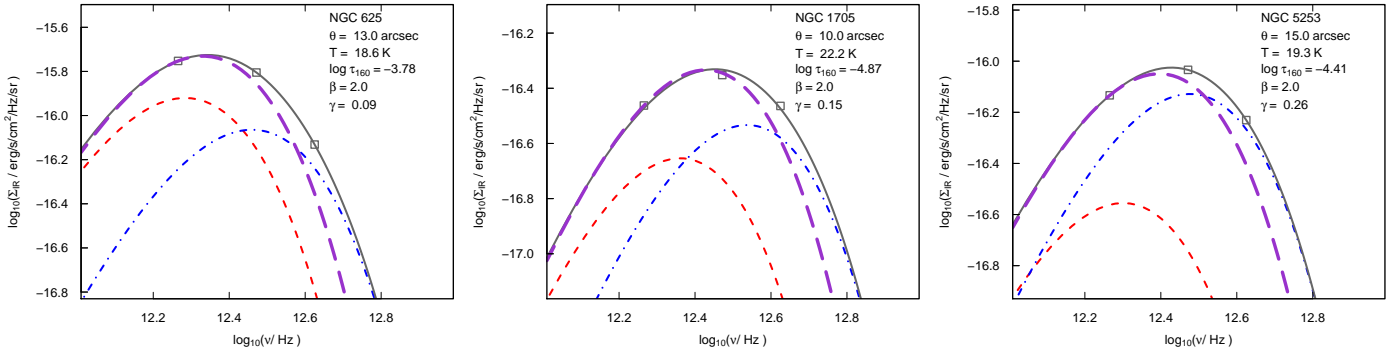
Figure 5 shows representative MBB-2T fits of the three targets, with nonzero  $\gamma$  values. The gray (solid) curve shows the best MBB-2T fits, while the long-dashed (purple) curves the single-temperature MBB fit with  $T = T_{\text{dust}}$ . The advantage of the two-temperature fits is evident by comparing the long-dashed MBB with  $T_{\text{dust}}$  to the combined MBB-2T solid curve; the single-temperature fit misses the high-frequency contribution from the warmer dust.

The MBB-T2 fits are numerically nontrivial. We left  $\gamma$  unconstrained, and in some cases, the fitted  $\gamma < 0$  or  $\gamma > 1$ . In those cases, an MBB fit (with  $\gamma = 0$ , by definition) was applied with  $\beta = 2.0$  as for the other MBB-T2 fits. This condition occurred for (45, 0, 33) individual resolution elements in NGC (625, 1705, 5253). Since rebinning to ( $13''$ ,  $10''$ ,  $15''$ ) for NGC (625, 1705, 5253), respectively, gives (77, 33, 90) resolution elements with PACS fluxes greater than the background, there are (58%, 0, 37%) of the fitted resolution elements with single-T MBB fits.

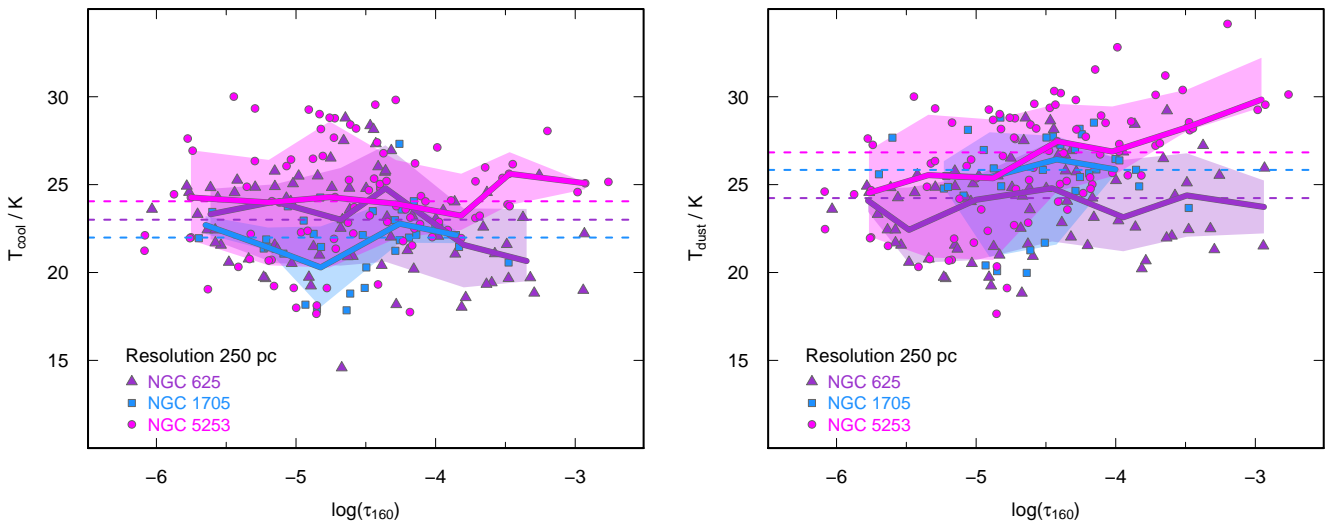
Given that the expected uncertainty in the individual PACS photometry is  $\sim 10\%$ , the rms values of both MBB and MBB-2T fits are quite good, and, except for NGC 1705, well within the expected uncertainties. Moreover, as shown in Appendix A, the MBB-2T fits are overall superior to MBB, possibly due to the extra fitted parameter and the consequent zero degrees of freedom. More details of the fits to the PACS data to derive  $\tau_{160}$  are given in Appendix A.

Figure 6 compares the best-fit  $T_{\text{cool}}$  with dust optical depth,  $\tau_{160}$  (left panel), and with  $T_{\text{dust}}$  versus  $\tau_{160}$  (right). We initially expected that  $T_{\text{cool}}$  might correlate with  $\tau_{160}$ ; however as shown in the left panel of Fig. 6, it does not. The range of  $T_{\text{cool}}$  is relatively narrow, a standard deviation of  $2$ – $3$  K, over a 3-order of





**Fig. 5.** Representative fits of Eq. (3) with significant  $\gamma$  values to illustrate the importance of two temperatures in the fitting function. The long-dashed red curves show the MBB with  $T_{\text{cool}}$ , the dot-dashed blue curves  $T_{\text{warm}}$ , and the gray (solid) ones the overall best fit. The (heavy) purple long-dashed curve corresponds to a single-temperature MBB with  $T_{\text{dust}}$ , normalized to the 160  $\mu\text{m}$  data point. For  $\gamma > 0$ , the simple MBB is clearly missing the contribution toward higher frequencies caused by warm dust at  $T_{\text{warm}}$ .



**Fig. 6.** Dust temperatures plotted against  $\tau_{160}$  for the 250 pc regions within the target galaxies: in the left panel best-fit  $T_{\text{cool}}$  and in the right panel effective temperature  $T_{\text{dust}}$ . The medians binned in  $\log_{10}(\tau_{160})$  are shown as heavy lines characterized by different colors, with the  $1\sigma$  variation by shaded regions. The horizontal dashed lines correspond to the overall  $T_{\text{cool}}$  galaxy medians (left panel) and  $T_{\text{dust}}$  (right). Only in the case of NGC 5253 does the effective temperature  $T_{\text{dust}}$  present a trend with  $\tau_{160}$ , in the sense that more optically thick regions show higher temperatures.

magnitude range of  $\tau_{160}$ . Moreover, the median cool-dust temperatures of the three targets do not differ significantly, given the 2–3 K spread: we find  $T_{\text{cool}} = (23.0, 22.0, 24.1)$  K for NGC (625, 1705, 5253), respectively. These temperatures are toward the high end of the temperature range of cool dust in normal, star-forming spirals (e.g., Galametz et al. 2012).

Kirkpatrick et al. (2014) found that  $T_{\text{cool}}$  is partly driven by star-formation activity, so that higher temperatures would be found for more intense SFRs, consistent with the starburst nature of our targets. Moreover, as shown in the right panel of Fig. 6, in NGC 5253, the effective temperature  $T_{\text{dust}}$  is correlated with  $\tau_{160}$  although the other two galaxies show little trend. Thus, in extreme dusty starbursts such as NGC 5253, warmer dust is associated with higher  $\tau_{160}$ .

#### 4.2. Infrared opacity and atomic gas surface density

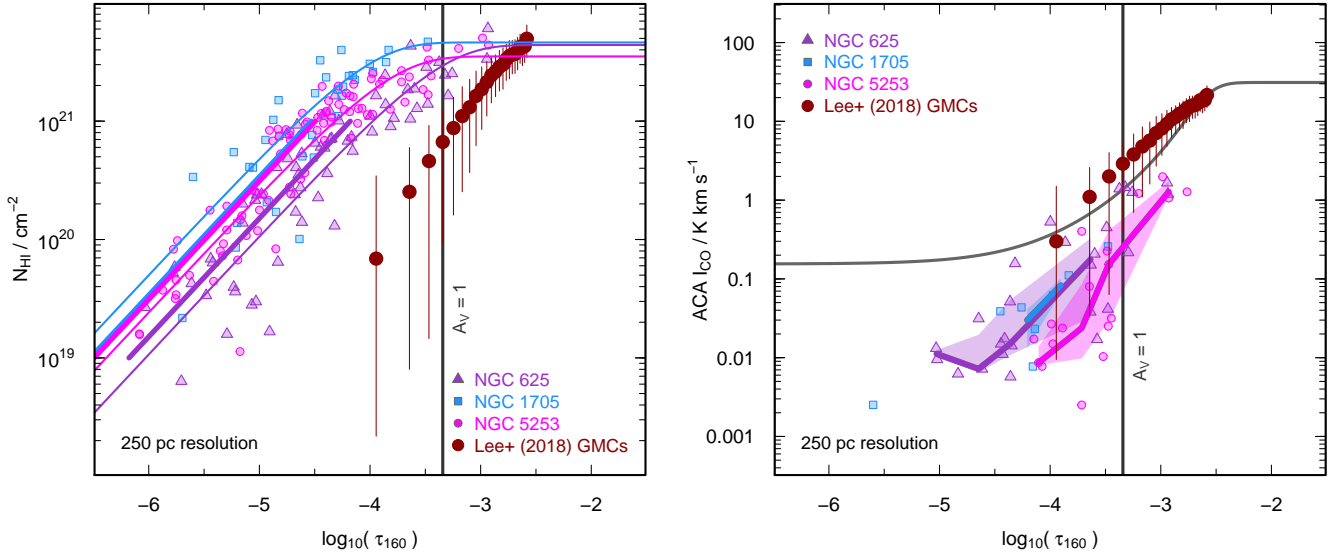
Atomic gas is an important part of the overall gas budget, especially in dwarf galaxies (e.g., Hunt et al. 2020). Comparing atomic gas surface density with a measurement of dust opacity enables an estimate of the dust-to-gas ratio (DGR), as well as an assessment of the overall association of dust content with HI.

Figure 7 (left panel) shows the trend of HI column density  $N_{\text{HI}}$  with  $\tau_{160}$  determined in the previous section; only points with signal-to-noise  $S/N \geq 3$  are shown. The data show a fairly tight correlation, but with an inflection or flattening at  $\tau_{160} \sim 10^{-4}$ . This is due to the “saturation” of  $N_{\text{HI}}$  at high column densities where most of the hydrogen has transitioned to molecular form, traceable by CO. Such a correlation between spatially-resolved dust content and HI is common in HI-dominated dwarf galaxies (e.g., Leroy et al. 2009), but is not generally observed in spirals (e.g., Hughes et al. 2014; Casasola et al. 2022).

We assume that for dark clouds with large  $\tau_{160}$  there is a finite amount of HI in the cloud “skin”, and that the cloud chemistry limits the amount of HI (see also Pineda et al. 2008). Thus, we can write:

$$N_{\text{HI}} = N0_{\text{HI}} \left(1 - e^{-k_{\text{HI}} \tau_{160}}\right), \quad (5)$$

where  $N0_{\text{HI}}$  is the HI column density at saturation, and  $k_{\text{HI}}$  defines the transition threshold for the dust optical depth  $\tau_{160}$  where saturation onsets. The best fits to this function are shown as curves in the left panel of Fig. 7; only points with HI signal-to-noise ( $S/N$ )  $\geq 3$  are included in the fits. We will incorporate  $k_{\text{HI}}$  to estimate  $X_{\text{CO}}$  from  $A_V$  in Sect. 5.



**Fig. 7.** Atomic gas column density  $N_{\text{HI}}$  versus  $160\mu\text{m}$  optical depth  $\tau_{160}$  (left panel) and CO ACA (velocity-integrated)  $T_{\text{B}}$  versus  $\tau_{160}$  (right). Only regions with  $S/N \geq 3$  are shown (and included in the fits). The best-fit linear relations (Eq. (6)) for  $\tau_{160}$  as a function of  $N_{\text{HI}}$  are shown as heavy curves (in log space), and only consider the points with  $10^{19} \leq N_{\text{HI}} \leq 10^{21} \text{ cm}^{-2}$  because of the need to consider the regions dominated by HI. The lighter curves show the fit to Eq. (5) as described in the text, and are used to determine  $A_V^{\text{HIcrit}}$ . Also shown are the GMCs from Lee et al. (2018) assuming  $A_V/\tau_{160} = 2200$  for consistency with their paper. The vertical line shows the equivalent of  $A_V = 1$  assuming this conversion. The heavy (colored) curves in the right panel correspond to  $I_{\text{CO}}$  binned in  $\log(\tau_{160})$ , and the gray curve is the fit from Lombardi et al. (2006) for CO in the MW Pipe Nebula GMC versus  $A_V$  converted to  $\tau_{160}$  as above (see also the study Pineda et al. 2008, on the Perseus molecular cloud complex).

Following Leroy et al. (2009) and Bolatto et al. (2011), we estimate the DGR from  $\tau_{160}$  and the total gas column density,  $N_{\text{HI}} (N_{\text{HI}} \equiv N_{\text{HI}} + 2N_{\text{H}_2})$ , by fitting a linear relation:

$$\tau_{160} = \delta_{\text{DGR}} N_{\text{gas}}, \quad (6)$$

where  $\delta_{\text{DGR}}$  is the slope of the relation, namely the DGR, and  $N_{\text{HI}}$  is in units of column density  $\text{cm}^{-2}$ . Here the underlying assumption is that this relation holds at all column densities. Thus, we can first calibrate it on HI, by restricting the fit to low column densities where  $N_{\text{HI}}$  is dominated by HI, and then extrapolate it to HI+H<sub>2</sub>. The fit of Eq. (6) was applied to HI columns with  $19 \leq \log(N_{\text{HI}}/\text{cm}^{-2}) \leq 21$ ; only points with signal-to-noise ( $S/N$ )  $\geq 3$  are included in the fit. We also performed fits with a nonzero intercept  $\tau_0$ , and found that it is always 0 to within the uncertainties; thus we fixed  $\tau_0$  to 0 to ensure a more reliable estimation of  $\delta_{\text{DGR}}$ .

As shown in Fig. 7, these linear fits well approximate the trend of  $\tau_{160}$  and HI at low column densities where HI dominates the gas budget. The best-fit  $\delta_{\text{DGR}}$  in Eq. (6) corresponds to  $\langle \tau_{160}/N_{\text{HI}} \rangle$  and differs slightly for the three galaxies, in qualitative agreement with what we would expect considering the albeit small metallicity differences (e.g., Rémy-Ruyer et al. 2014, see Table 1):

$$\delta_{\text{DGR}} = \begin{cases} (6.6 \pm 0.4) \times 10^{-26} \text{ cm}^2 & \text{NGC 625} \\ (3.0 \pm 0.5) \times 10^{-26} \text{ cm}^2 & \text{NGC 1705} \\ (3.2 \pm 0.2) \times 10^{-26} \text{ cm}^2 & \text{NGC 5253.} \end{cases} \quad (7)$$

These values are 3–5 times lower than  $\tau_{160}/N_{\text{H}} = 1.61 \times 10^{-25} \text{ cm}^{-2}/\text{H}$ , found in the local diffuse ISM by Hensley & Draine (2021), roughly consistent with the linear trend with the  $\sim \frac{1}{3} - \frac{1}{4} Z_{\odot}$  metallicities of our targets. The values for our dwarf starbursts are also comparable with  $\delta_{\text{DGR}}$  for N83, with O/H of  $\sim \frac{1}{5} Z_{\odot}$  (e.g., Berg et al. 2012), in the Small Magellanic Cloud (SMC):  $\tau_{160} = 2.3\text{--}4.3 \times 10^{-26} N_{\text{gas}}/\text{cm}^{-2}$

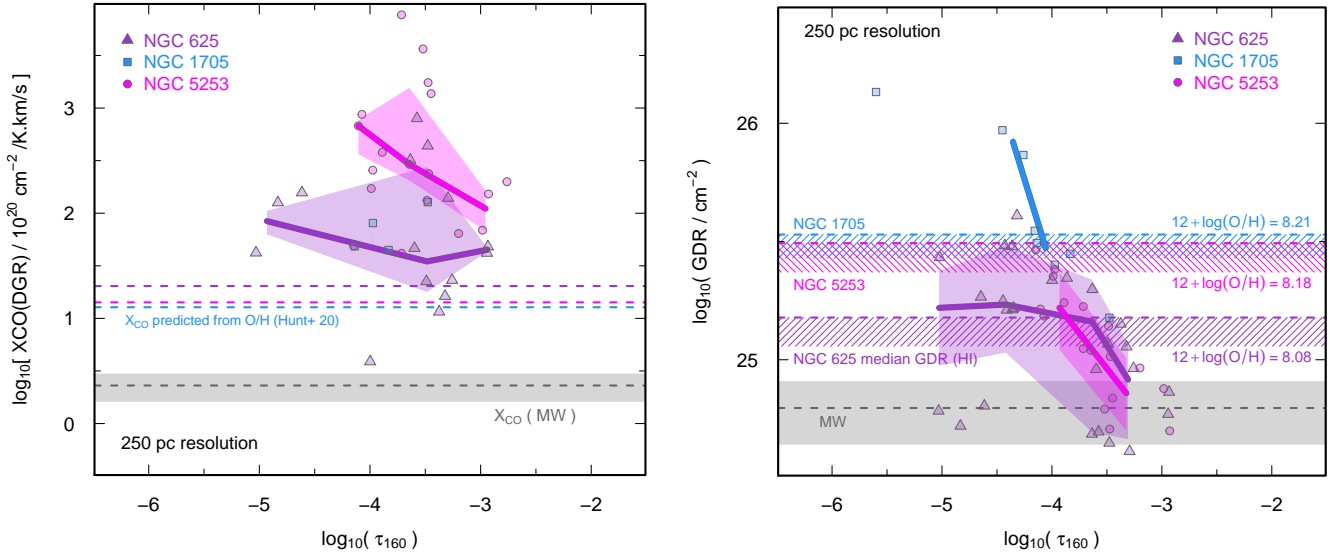
(Bolatto et al. 2011), where we have reported their 36% correction for helium to our convention without the helium correction (see also Leroy et al. 2009).

In the limit of the HI-dominated regime at low  $\tau_{160}$ , Eq. (5) should converge to Eq. (6) with  $\delta_{\text{DGR}} = 1/(N_{\text{OHI}} k_{\text{HI}})$ . Thus, in principle, we could have used the fits of Eq. (5) to infer  $\delta_{\text{DGR}}$ , rather than Eq. (6). However, Fig. 7 shows offsets of 30–40% between the two estimates, so it is unclear which to prefer. After error propagation, the uncertainties on  $\delta_{\text{DGR}}$  from the fits of Eq. (5) are larger than those given in Eq. (7), so we prefer to adopt the results from fitting Eq. (6) with only one free parameter and over the range in column density dominated by HI.

The DGR  $\delta_{\text{DGR}}$  is given in units of optical depth per H, because we want to compare dust columns with gas columns. Although it would be preferable to determine the DGR for individual regions (e.g., Bolatto et al. 2011; Sandstrom et al. 2013), this is difficult for our dwarf targets. The small number of individual resolution elements within each galaxy effectively precludes a statistically relevant spatially-resolved DGR determination. Thus, we use an average DGR determined from the data as shown in the left panel of Fig. 7. This point is further discussed in Sect. 7.

#### 4.3. Molecular gas surface density, $\tau_{160}$ , and $X_{\text{CO}}$ at 250 pc resolution

The trend of CO velocity-integrated brightness temperature observed with ACA at  $\sim 250$  pc resolution is shown in the right panel of Fig. 7. Also shown are the giant molecular clouds (GMCs) in the Milky Way (MW) studied by Lee et al. (2018), where they estimate  $A_V$  from  $\tau_{850}$ . As for HI,  $I_{\text{CO}}$  in units of  $\text{K km s}^{-1}$  correlates with dust opacity, although with somewhat larger scatter than for HI. At a given  $\tau_{160}$ , our low-metallicity starbursts show lower surface brightness CO emission than the MW GMCs. Part of this may be due to the much higher resolution in the MW observations (1 pc; Lee et al. 2018), relative to



**Fig. 8.** Left panel: Inferred  $X_{\text{CO}}$  conversion factor from Eq. (8) as a function of  $\tau_{160}$ . Also shown are values that would be estimated from the metallicity dependence found by Hunt et al. (2020) as  $X_{\text{CO}} \propto Z^{-1.55}$  (see also Accurso et al. 2017). Heavy curves show the medians in  $\log_{10}(\tau_{160})$  for each galaxy (except for NGC 1705 for which there are too few points), and the shaded regions indicate  $1\sigma$  standard deviations. Right panel: GDR (here we are using the inverse of  $\delta_{\text{DGR}}$ ) that would be inferred assuming the metallicity dependence of the  $X_{\text{CO}}$  conversion factor found by Hunt et al. (2020). The range of GDRs estimated by different methods is shown as the hatched horizontal strips. As in the left panel, heavy curves show the medians, and shaded regions the  $1\sigma$  standard deviation.

the 250 pc regions studied here. However, another part of this stems from the  $X_{\text{CO}}$  factor needed to bring observed CO brightness temperatures to gas column densities.

We now have the necessary ingredients to infer  $N_{\text{H}_2}$  from  $N_{\text{HI}}$  and  $\delta_{\text{DGR}}$ , using the following expression:

$$N_{\text{H}_2}^{\text{DGR}} = \frac{1}{2} \left( \frac{\tau_{160}}{\delta_{\text{DGR}}} - N_{\text{HI}} \right), \quad (8)$$

where  $\delta_{\text{DGR}}$  is determined from the fit of Eq. (6). For each 250 pc resolution element, we can derive  $N_{\text{H}_2}^{\text{DGR}}$ , and then use  $I_{\text{CO}}$  to find the local  $X_{\text{CO}} = I_{\text{CO}}/N_{\text{H}_2}^{\text{DGR}}$ . To include a resolution element in this estimate, we require that both HI and CO binned data points have  $S/N \geq 3$ . Thus, instead of the (70, 33, 90) 250 pc PACS resolution elements for the determination of  $\tau_{160}$  for NGC (625, 1705, 5253), respectively, the numbers are now reduced to (26, 8, 18) usable elements for the three galaxies. However, a small fraction of these gives negative values of  $N_{\text{H}_2}$  in Eq. (8), because the HI column density slightly exceeds what would be inferred from the ratio,  $\tau_{160}/\delta_{\text{DGR}}$ . This could be a consequence of our assumption of a global DGR, as also discussed in Sect. 7. In any case, the number of regions useful for the calculation of  $X_{\text{CO}}$  dwindles further to (20, 4, 17) for NGC (625, 1705, 5253), respectively.

The results are shown in the left panel of Fig. 8, where also illustrated are the metallicity-dependent predictions for global  $X_{\text{CO}}$  [ $X_{\text{CO}} \propto (Z/Z_{\odot})^{-1.55}$ ] according to Hunt et al. (2020). The DGR-inferred  $X_{\text{CO}}$  values sometimes exceed the expectation from the metallicity dependence, in some cases by an order of magnitude or more. The large scatter precludes definitive statements, but the main point that emerges from Fig. 8 is that a simple metallicity dependence does not explain the  $X_{\text{CO}}$  factors derived from the DGR on 250 pc scales.

To investigate this further, and check for consistency, the right panel of Fig. 8 shows the gas-to-dust ratios (GDRs) that would be inferred if we had assumed a metallicity-dependent  $X_{\text{CO}}$ . The plotted GDRs are simply the inverse of  $\delta_{\text{DGR}}$  that were derived in Eq. (6), and the hatched areas show the range of

GDRs estimated by different methods. At  $\tau_{160} \lesssim 10^{-4}$ , where the gas budget is dominated by HI, the inferred GDRs more or less conform to expectations. However, for higher  $\tau_{160}$ , where  $\text{H}_2$  inferred from CO starts to impact the gas content, the GDRs are lower, reaching MW values at  $\tau_{160} \sim 10^{-3}$ . Such behavior is consistent with the left panel of Fig. 8 where  $X_{\text{CO}}$  computed from the DGRs are higher than what would be expected from the global metallicity dependence found by Hunt et al. (2020). This point will be explored in Sect. 6.

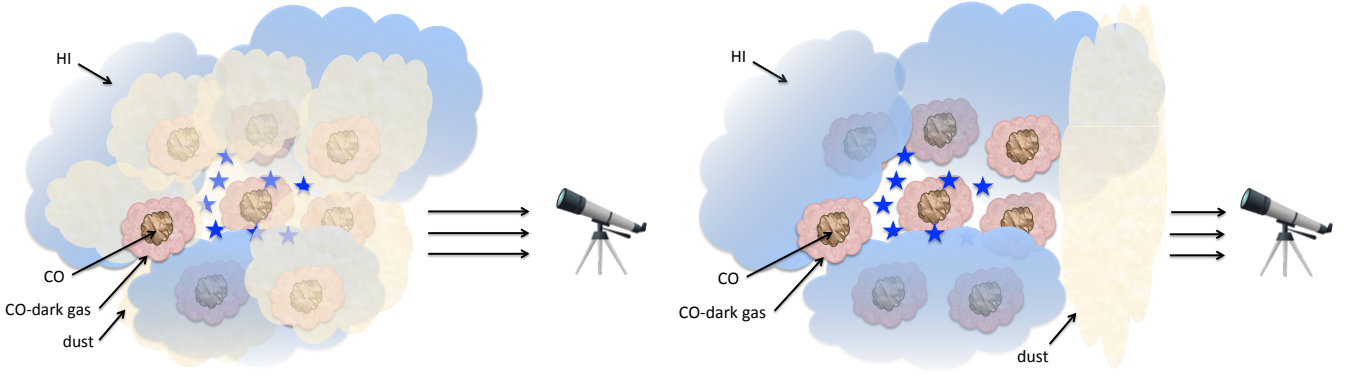
## 5. Small-scale dust extinction, molecular gas content, and the $X_{\text{CO}}$ conversion factor

We now turn to the ALMA 12-m data with a higher resolution,  $\sim 40$  pc. Dust columns at this resolution are inferred from foreground visual reddening,  $E(B - V)$ , estimated from the Balmer decrement from the MUSE maps. We convert  $E(B - V)$  to  $A_V$  by assuming  $A_V/E(B - V) = 3.1$  (e.g., Draine 2003). The problem with tracing dust extinction through  $A_V^{\text{MUSE}}$  from the Balmer decrement is that  $A_V$  gives attenuation rather than the true visual optical depth  $\tau_V$ . Moreover, the attenuation  $A_V^{\text{MUSE}}$  is due only to dust in front of the ionized gas, whereas  $\tau_{160}$  measures all of the dust along the line of sight. More generally, we need to distinguish between dust attenuation from  $A_V^{\text{MUSE}}$  and true visual optical depth (e.g., Boquien et al. 2013). In the following, we quantify this distinction and show that  $A_V^{\text{MUSE}}$  from the Balmer decrement does not always directly trace  $\tau_V$  in these low-metallicity starbursts.

### 5.1. Visual attenuation versus extinction and dust optical depth

Assuming that the extinguishing dust is placed in a foreground screen, the relation between attenuation and dust optical depth is simple:

$$A_V = -2.5 \log_{10}(e^{-\tau_V}) = 1.086 \tau_V. \quad (9)$$



**Fig. 9.** Left panel: Idealized cartoon illustrating the mixed configuration of dust, stars, and gas. Right panel: The same but with the foreground screen configuration. The amount of dust in the screen in the right panel is assumed to be roughly half of the total dust shown in the left panel. While the infrared  $\tau_{160}$  penetrates the full dust column along the line of sight, the optical depth inferred from the Balmer decrement only captures the dust between the stars that ionize the gas and the observer.

Thus, the attenuation  $A_V$  is exactly proportional to the dust optical depth  $\tau_V$ . However, assuming that the dust is uniformly mixed with the emitters gives a slightly more complicated relation:

$$A_V = -2.5 \log_{10} \left( \frac{1 - e^{-\tau_V}}{\tau_V} \right). \quad (10)$$

Figure 9 illustrates these two configurations of the dust. The infrared optical depth traced by  $\tau_{160}$  penetrates the full dust column along the line of sight, while extinction given by the Balmer decrement only probes the dust between the observer and the ionized gas. The assumption that the dust is uniformly mixed with the ionized gas is an approximation, but, as shown in the figure, has the advantage of being slightly more realistic from a physical point of view.

As described by Natta & Panagia (1984), Disney et al. (1989), and others (e.g., Witt & Gordon 1996, 2000), solutions can be obtained for even more complex assumptions on the relative geometry of the dust and the emitting regions. In any case, the problem that emerges is the derivation of  $\tau_V$  from  $A_V$  in more complex geometries of the dust relative to the emission source. Equation (10) provides a fortunate example because it is invertible using the Lambert W function as shown by Boquien et al. (2013)<sup>6</sup>:

$$\tau_V = W(-10^{0.4A_V} e^{-10^{0.4A_V}}) + 10^{0.4A_V}. \quad (11)$$

Here we make the assumption that the dust is uniformly mixed with the ionized gas, namely that Eq. (10) is a better description of the dust column  $\tau_V$  than Eq. (9), at least for our use of the Balmer-decrement derived  $A_V^{\text{MUSE}}$  to infer dust columns. We calculate  $\tau_V$  under this assumption and compare it with what would be inferred by simply equating  $\tau_V$  with  $A_V$  (with a small proportional factor) as in Eq. (9).

The comparison of  $A_V$  and  $\tau_V$  (Eqs. (10), (11)) under the assumption of dust uniformly mixed with the ionized gas emission is shown in Fig. 10. The dashed curve shows the analytical solution, while the solid line indicates  $y = \log_{10}(\tau_V) = x - \log_{10}(1.086) + \log_{10}(2)$ , where  $x = \log_{10}(A_V^{\text{MUSE}})$ . The factor of 2 takes into account that  $A_V^{\text{MUSE}}$  only probes the extinction along the line of sight, i.e., the front of the foreground screen (see above), and the other factor is from Eq. (9). Indeed, for

<sup>6</sup> The Lambert W function provides the solution  $y$  of  $x = y e^y$ , where  $x = -10^{0.4A_V} e^{-10^{0.4A_V}}$  and  $y = \tau_V - 10^{0.4A_V}$ .

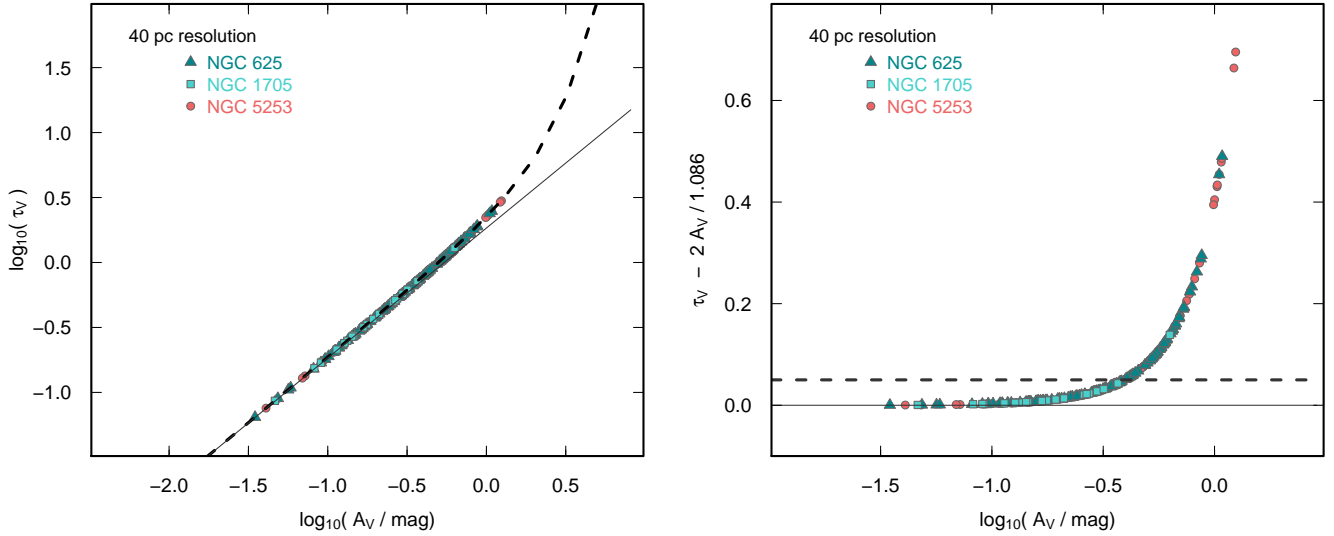
small  $\tau_V$ , Eq. (10) reduces to  $A_V \approx 1.086 (\tau_V/2)$ . The difference of the two quantities  $\tau_V$  and  $y$  from  $A_V^{\text{MUSE}}$  is negligible at low  $\tau_V$ , but becomes significant ( $\gtrsim 25\%$ ) for  $A_V^{\text{MUSE}} \gtrsim 0.3-0.5$  mag. At  $A_V$  higher than this,  $\tau_V$  becomes clearly the better tracer of dust opacity since the assumption of a foreground screen progressively fails at high dust columns. Our preference for  $\tau_V$  is also supported by the comparison with Galactic GMCs as discussed in the next section (see Fig. 11).

## 5.2. CO brightness temperature and visual extinction at 40 pc resolution

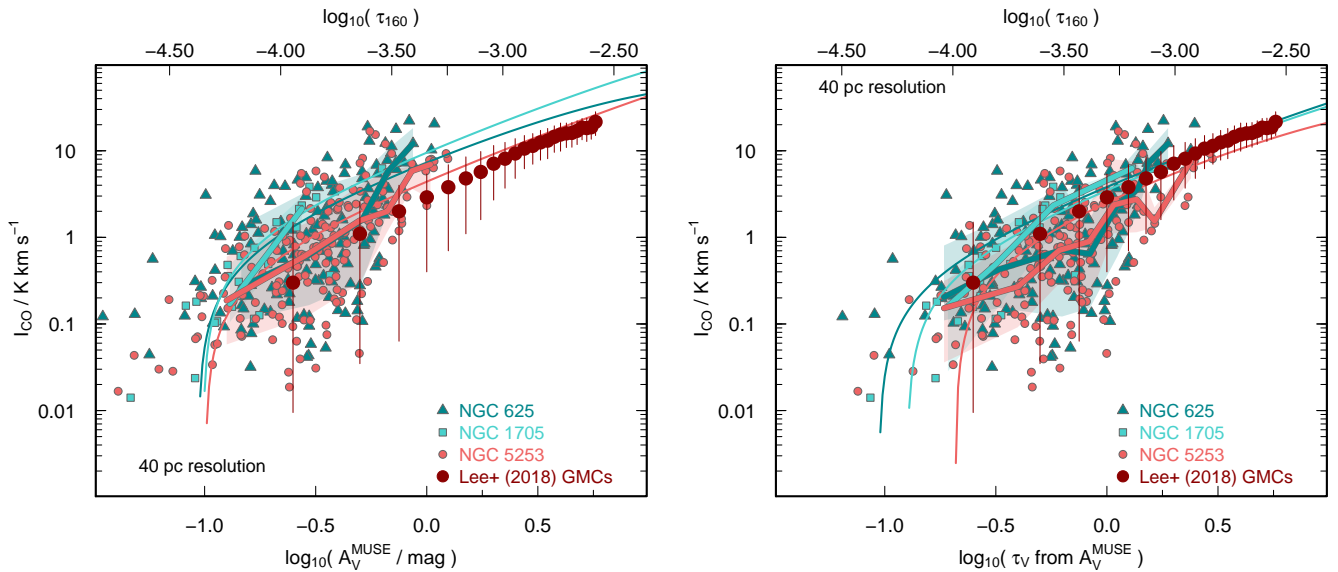
Figure 11 shows the 12-m data plotted in the left panel against  $A_V^{\text{MUSE}}$ , calculated from  $E(B - V)$  and in the right against  $\tau_V$  inferred from Eq. (11). Both data sets have been rebinned to  $2''$  (corresponding to  $\approx 40$  pc, see Table 1). Like the trend of  $I_{\text{CO}}$  with  $\tau_{160}$  at 250 pc resolution,  $I_{\text{CO}}$  at 40 pc also varies systematically with  $A_V$  and  $\tau_V$ , albeit with significant scatter.

Figure 11 shows that the 40 pc CO-emitting regions have higher brightness temperatures than the  $\sim 250$  pc regions shown in (the right panel of) Fig. 7. Indeed, the surface brightness of CO in our targets at the two resolutions sampled here is very different. Comparison of Figs. 7 and 11 illustrates that  $I_{\text{CO}}$  of the brightest CO-emitting regions that are visible at high dust columns, traced by either  $\tau_{160}$  or  $\tau_V$ , are a factor of  $\sim 10$  higher at 40 pc than 250 pc. This is consistent with beam dilution of a given molecular gas surface density because the ratio of the beam area is  $(250/40)^2 \sim 40$ . Such behavior is not surprising because we expect CO to be highly clumped on these scales, much more so than HI (Leroy et al. 2013). It also tells us that for probing CO emission in low-metallicity galaxies, large beams, with single-dish observations at the extreme end, are not as effective as beams on scales of (at least) a few tens of parsecs; they are unable to trace the high-density CO columns. This means that single-dish efforts to detect CO at low metallicity may be doomed to fail at the outset because of beam dilution, a point that was also made by Rubio et al. (1993) in a pioneering paper using SEST observations of the SMC. We explore this further in Sect. 6.

Also shown in Fig. 11 are the CO velocity-integrated brightness temperatures of the GMCs in our Galaxy studied at  $\sim 1$  pc resolution by Lee et al. (2018). They infer  $A_V$  from  $E(B - V)$ , (also using  $A_V/E(B - V) = 3.1$ ) derived from the dust optical depth at  $850 \mu\text{m}$   $\tau_{850}$  as measured by *Planck*.



**Fig. 10.** Relations between  $A_V$  and  $\tau_V$ . Left panel:  $\tau_V$  inferred from Eq. (11) for the targets plotted against  $\log_{10}(A_V^{\text{MUSE}})$ . The heavy dashed curve shows the true solution, and the lighter weight solid curve shows not identity, but rather  $y = \log_{10}(\tau_V) = x - \log_{10}(1.086) + \log_{10}(2)$ , where  $x = \log_{10}(A_V^{\text{MUSE}})$ . The factor of 2 takes into account that  $A_V^{\text{MUSE}}$  only probes the extinction along the line of sight, i.e., the front of the foreground screen, and the other factor is from Eq. (9). The difference of the two quantities  $\tau_V$  and  $A_V^{\text{MUSE}}$  is negligible at low  $\tau_V$ , but becomes significant for  $A_V^{\text{MUSE}} \gtrsim 0.3 - 0.5$  mag. At  $A_V^{\text{MUSE}} > 1$  mag,  $\tau_V$  “runs” away, relative to  $A_V$ . Right panel: Residuals of  $\tau_V - 2A_V^{\text{MUSE}}/1.086$  versus  $\log(A_V)$ . Although difficult to appreciate in the left panel, 34% of the data points have residuals  $>0.05$ , marked by the horizontal dashed line.



**Fig. 11.** CO velocity-integrated  $T_B I_{\text{CO}}$  plotted versus (logarithm) visual extinction  $A_V$  (left panel) and (logarithm) visual dust optical depth  $\tau_V$  (right). The top axes show the scale for  $\tau_{160}$  assuming that  $A_V/\tau_{160} = 2180$ , as described in Sect. 5.3. The light curves show fits to Eq. (12). Heavy curves show the medians for each galaxy binned in  $\log_{10}(A_V)$ , (left),  $\log_{10}(\tau_V)$ , (right), with the shaded regions corresponding to  $\pm 1\sigma$  deviations. Also shown in both panels are the MW GMCs studied by Lee et al. (2018), with  $A_V$  inferred from *Planck*; see Sect. 5 for more details.

(Sub)Millimeter/far-infrared optical depths such as  $\tau_{850}$  (and even  $\tau_{160}$ ) make emission at these wavelengths optically thin tracers of dust, better probing the entire line of sight through dust and gas. Comparison of the Lee et al. (2018) GMCs with our CO data is enlightening. If we assume that  $A_V^{\text{MUSE}}$  (left panel in Fig. 11) measured from the Balmer decrement is identical to  $A_V$  inferred from  $\tau_{850}$ , at a given  $A_V$ , we would deduce that the GMC CO 1 pc column densities are lower than those found for our low-metallicity starbursts on  $\sim 40$  pc scales. However, in the right panel where  $\tau_V$  is plotted rather than  $A_V^{\text{MUSE}}$ , for a given  $\tau_V$ , the CO integrated brightness temperatures of the GMCs (with their  $A_V$  taken to be equivalent to our  $\tau_V$ ) coincide very well

with the CO emission observed at 40 pc resolution. This is an indication that the assumption that the obscuring dust measured by  $A_V^{\text{MUSE}}$  is mixed with the ionized gas, with an optical depth of  $\tau_V$ , is better than assuming that the dust is a foreground screen. This is true for the low-metallicity starbursts studied here, but the differences would even be more profound for galaxies with larger dust content.

However, that the 40 pc integrated brightness temperatures of our targets are similar the GMCs in the MW observed at 1 pc resolution by Lee et al. (2018) is surprising. The GMCs would have been expected to show significantly higher surface brightness within the much smaller beam. Instead, our finding would imply

that the CO clumps within the 40 pc beam are of much higher surface brightness than the GMCs measured by Lee et al. (2018), consistent with the idea that the only CO-emitting regions that remain at low metallicity are the dense cores that are sufficiently shielded to avoid photodissociation.

As discussed by Lee et al. (2018), there are at least two features in the  $I_{\text{CO}}$  versus  $A_V$  ( $\tau_V$ ) relation that would be expected from a theoretical point of view. The first is a CO-formation visual extinction threshold, below which CO emission plummets because of photodissociation of the CO molecules (e.g., van Dishoeck & Black 1988; Bell et al. 2006; Visser et al. 2009; Glover & Mac Low 2011; Shetty et al. 2011). This would be reflected in the presence of carbon emitting as  $\text{C}^+$  or  $\text{C I}$  in parts of the molecular clouds where CO is insufficiently shielded (e.g., Hollenbach & Tielens 1997; Papadopoulos et al. 2004; Wolfire et al. 2010).

Another feature expected theoretically is a flattening at high  $A_V$  ( $\tau_V$ ) where CO emission saturates, becoming optically thick (e.g., Glover & Mac Low 2011; Shetty et al. 2011). Such a feature is observed in some GMC ensembles in the MW, where there is clear plateau for  $A_V \gtrsim 1$  mag (e.g., Lombardi et al. 2006; Pineda et al. 2008).

To test for these features in the 40 pc resolution  $I_{\text{CO}}$ ,  $A_V$  ( $\tau_V$ ) relation for low-metallicity starbursts, we have fit the points in Fig. 11 with a function similar to that of Eq. (5) of the form:

$$I_{\text{CO}} = W_{0\text{CO}} \left( 1 - e^{-k_{\text{CO}} (A_V - A_V^{\text{CO,thresh}})} \right), \quad (12)$$

where  $W_{0\text{CO}}$  is the velocity-integrated CO brightness temperature at saturation;  $k_{\text{CO}}$  defines the transition threshold for the dust optical depth  $\tau_V$  where saturation sets on; and  $A_V^{\text{CO,thresh}}$  gives the onset for CO emission. As before, only points with signal-to-noise ( $S/N$ )  $\geq 3$  are included in the fits. The best fits to this function are shown as curves in Fig. 11; in the right panel we have substituted  $\tau_V$  for  $A_V$  in Eq. (12). The results of the fits and the visual inspection of the plots show that the saturation feature at high  $\tau_V$  is not visible in our data;  $W_{0\text{CO}}$  and  $k_{\text{CO}}$  are ill-determined both for the plots using  $A_V$  and those with  $\tau_V$ . Instead, the  $A_V^{\text{CO,thresh}}$  parameter is somewhat better determined with:

$$A_V^{\text{CO,thresh}} = \begin{cases} 0.09 \pm 0.06 \text{ mag} & \text{NGC 625} \\ 0.10 \pm 0.02 \text{ mag} & \text{NGC 1705} \\ 0.11 \pm 0.05 \text{ mag} & \text{NGC 5253.} \end{cases} \quad (13)$$

The results for  $A_V^{\text{CO,thresh}}$  using  $\tau_V$ , rather than  $A_V$ , have somewhat higher values, although with slightly larger uncertainty. In any case, our 40 pc CO data show no evidence for a flattening at high  $\tau_V$ , but some tentative indication of an  $A_V$  CO threshold of  $\sim 0.1$  mag. This is a much lower value than given by the simulations of Glover & Clark (e.g., 2016) that predict a steep reduction for  $A_V \lesssim 1$  mag; however, their simulations are at much finer (0.06 pc) resolution than our observations, so may not be directly comparable. Our value of  $A_V^{\text{CO,thresh}} \approx 0.1$  mag is also roughly ten times lower than found by Pineda et al. (2008) with  $A_V^{\text{CO,thresh}}$  generally  $\gtrsim 1$  mag for their sample of (solar metallicity) MW GMCs.

### 5.3. The $X_{\text{CO}}$ factor and visual optical depth

We can now infer the  $X_{\text{CO}}$  conversion factor at  $\approx 40$  pc resolution from  $\tau_V$  (or  $A_V$ ), similar to what we have done at lower resolution

( $\approx 250$  pc) with  $\tau_{160}$  in the previous sections. We write:

$$N_{\text{H}_2}^{\text{Av}} = \frac{1}{2} \left( \frac{N_{\text{H}}}{A_V} \right) \left[ 2 A_V^{\text{MUSE}} - A_V^{\text{Hcrit}} \right], \quad (14)$$

where  $N_{\text{H}}/A_V$  is the total column density of hydrogen atoms in either atomic or molecular form relative to visual extinction  $A_V$ . This approach follows Lee et al. (2018), but they probed  $A_V$  with dust emission, so we must make different assumptions for the dependence of  $N_{\text{H}_2}$  on  $A_V^{\text{MUSE}}$ . The multiplicative factor of 2 for  $A_V^{\text{MUSE}}$  in Eq. (14) is because our estimate of  $A_V^{\text{Hcrit}}$  relies on  $\tau_{160}$  which probes the entire line of sight, thus sampling the shielding layer on both the front and back sides of the medium; conversely  $A_V^{\text{MUSE}}$  is calculated assuming a foreground screen, thus sampling only the front side (see Lee et al. 2018). The  $A_V^{\text{Hcrit}}$  term takes into account the transition from HI to  $\text{H}_2$  at high dust and gas columns (e.g., Bigiel et al. 2008; Krumholz et al. 2009; Sternberg et al. 2014); it can be estimated from  $k_{\text{HI}}$  in the HI formulation of radiative transfer in Eq. (5), after converting the units to  $A_V \text{ mag}^{-1}$ . The analogous equation for  $\tau_V$  would be:

$$N_{\text{H}_2}^{\tau_V} = \frac{1}{2} \left( \frac{N_{\text{H}}}{\tau_V} \right) \left[ \tau_V - \tau_V^{\text{Hcrit}} \right], \quad (15)$$

where  $\tau_V^{\text{Hcrit}}$  is defined as  $1.086 A_V^{\text{Hcrit}}$ , and  $N_{\text{H}}/\tau_V$  is the equivalent of  $N_{\text{H}}/A_V$  but in units of  $\tau_V$ , under the assumption that the denominator measures the extinction in the dust along the line of sight. Equation (15) could be seen as inconsistent with our conclusion that the screen geometry for dust extinction is not an accurate description; however,  $\tau_V^{\text{Hcrit}}$  describes the impact of the conversion of  $\text{H}_2$  to HI on the extinction dependence of  $N_{\text{H}_2}$ , thus is not strictly related to the geometry of the dust relative to the ionized gas.

$N_{\text{H}}/A_V$  is a critical factor in our determination of  $X_{\text{CO}}$  from  $A_V$  on  $\sim 40$  pc scales, and it relies on several assumptions. Along diffuse lines of sight in the MW, Bohlin et al. (1978) find  $N_{\text{H}}/A_V = 1.87 \times 10^{21} \text{ cm}^{-2} \text{ mag}^{-1}$ . Assuming  $A_V/\tau_{160} = 2180$  (Hensley & Draine 2021), we can also estimate  $N_{\text{H}}/A_V$  from  $\delta_{\text{DGR}}$  at  $\sim 250$  pc resolution (see Fig. 7, Eq. (6)) measured for our targets. We find:

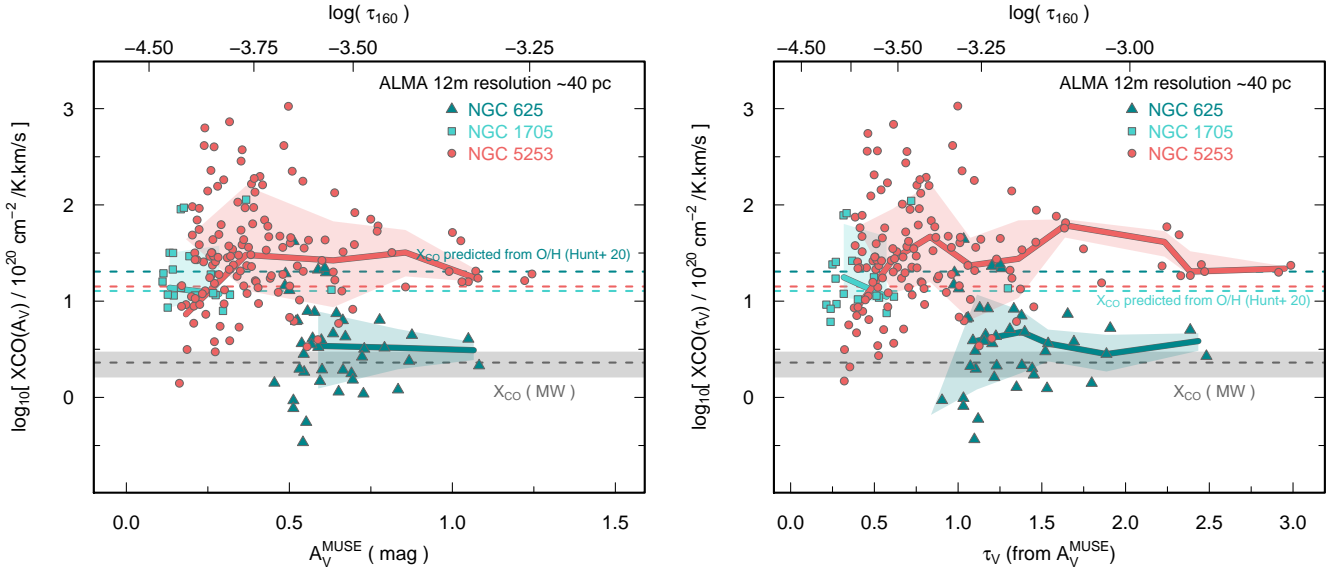
$$N_{\text{H}}/A_V = \begin{cases} (6.9 \pm 0.2) \times 10^{21} \text{ cm}^{-2} \text{ mag}^{-1} & \text{NGC 625} \\ (1.6 \pm 0.5) \times 10^{22} \text{ cm}^{-2} \text{ mag}^{-1} & \text{NGC 1705} \\ (1.4 \pm 0.4) \times 10^{22} \text{ cm}^{-2} \text{ mag}^{-1} & \text{NGC 5253.} \end{cases} \quad (16)$$

As shown in the right panel of Fig. 8, there is a relatively large spread in these estimates, ranging from  $\sim 0.2$  dex to 0.5 dex. In any case, at face value, the total gas-to-extinction ratios we measure for these low-metallicity galaxies are  $\approx 4$ –8 times higher than the MW value (e.g., Bohlin et al. 1978), qualitatively consistent with a linear metallicity scaling.

Another critical factor in our 40 pc formulation of  $N_{\text{H}_2}$  is  $A_V^{\text{Hcrit}}$ , which is directly related to  $k_{\text{HI}}$  in Eq. (5) as is the inflection where atomic gas transitions to  $\text{H}_2$ . Thus, with  $A_V/\tau_{160}$ , we calculate values of  $A_V^{\text{Hcrit}}$  for the low-metallicity starbursts:

$$A_V^{\text{Hcrit}} = \begin{cases} 0.90 \pm 0.21 \text{ mag} & \text{NGC 625} \\ 0.20 \pm 0.05 \text{ mag} & \text{NGC 1705} \\ 0.32 \pm 0.04 \text{ mag} & \text{NGC 5253.} \end{cases} \quad (17)$$

For NGC 1705 and NGC 5253, the  $A_V^{\text{Hcrit}}$  values are fairly low, as can also be seen by the curves in Fig. 7, while for NGC 625, the value is roughly 3 times higher, although also 4–5 times



**Fig. 12.**  $X_{\text{CO}}$  estimated from Eq. (14) is plotted as a function of  $A_V$  in the left panel, and of  $\tau_V$  in the right. As in Fig. 8, we include as horizontal dashed lines,  $X_{\text{CO}}$  that would be estimated from the metallicity dependence found by Hunt et al. (2020), as  $X_{\text{CO}} \propto Z^{-1.55}$ . The MW  $X_{\text{CO}} = 2.3 \times 10^{20} \text{ cm}^{-2} / \text{K km s}^{-1}$  is also given together with the uncertainties. Heavy curves show the medians for each galaxy binned in  $A_V^{\text{MUSE}}$  (left) and  $\tau_V$  (right) with shaded regions showing the  $1\sigma$  standard deviations.

more uncertain. The values for NGC 1705 and NGC 5253 of 0.2–0.3 mag are consistent with  $A_V^{\text{Hcrit}} = 0.2$  mag for a fixed radiation field found by Draine (1978), and by Krumholz et al. (2009), depending on dust properties.

Finally, both Eqs. (16) and (17) rely on the conversion of  $A_V$  to  $\tau_{160}$ . This conversion is uncertain, and different groups adopt a range of values. Leroy et al. (2009) use  $A_V/\text{mag} = 1910 \tau_{160}$ , while Lee et al. (2015) adopt  $A_V/\text{mag} = 2200 \tau_{160}$ . The higher dust temperatures and lower dust optical depth found by Planck Collaboration XI (2014) lead to  $A_V/\text{mag} = 3246 \tau_{160}$ , assuming  $E(B - V)/A_V = 3.1$  as done here. Here, we adopt  $A_V/\text{mag} = 2180 \tau_{160}$  (Hensley & Draine 2021), close to the Lee et al. (2015) value, but still somewhat subject to uncertainty.

These uncertainties in the ingredients for the calculation of  $N_{\text{H}_2}$  make our inference of  $X_{\text{CO}}$  subject to various caveats. Nevertheless, results are encouraging. Figure 12 shows  $X_{\text{CO}}$  computed using  $N_{\text{H}_2}$  inferred from Eqs. (14) and (15); the left panel shows  $X_{\text{CO}}$  versus  $A_V$  and the right versus  $\tau_V$ . Also shown in the figure are the expectations from the global metallicity dependence of  $X_{\text{CO}}$  from Hunt et al. (2020, see also Accurso et al. 2017). There is possibly less scatter in the right panel ( $\tau_V$ ), at least for NGC 5253, but overall the two plots show mutually consistent values of  $X_{\text{CO}}$ . While the median curve for NGC 5253 falls roughly where expected for consistency with a global metallicity dependence of  $X_{\text{CO}}$ , NGC 625 falls fairly close to the MW. This is unexpected given that NGC 625 has the lowest O/H of our sample, although the global O/H variations among the three targets are not large. The reason why NGC 625 shows  $X_{\text{CO}}$  at 40 pc resolution close to the Galactic value is the high value of  $A_V^{\text{Hcrit}}$  in Eq. (17). Given the relatively low signal-to-noise on the measurement of  $A_V^{\text{Hcrit}}$  for NGC 625, we have experimented with lower values of  $A_V^{\text{Hcrit}} \approx 0.2\text{--}0.3$ , and find that NGC 625 would fall closer to the global metallicity-dependent  $X_{\text{CO}}$  expectations, consistent with the other galaxies. Nevertheless, this would be a deviation of  $\geq 3\sigma$ , so we continue to consider the nominal  $A_V^{\text{Hcrit}}$  value for NGC 625.

## 6. Comparison of large- and small-scale $X_{\text{CO}}$

Figures 8 and 12 present two different pictures of the behavior of  $X_{\text{CO}}$ . At  $\sim 250$  pc resolution, conversion factors  $X_{\text{CO}}$  show large scatter, and are generally higher than what would be predicted from a simple metallicity dependence. Instead, with 12-m data at  $\sim 40$  pc resolution,  $X_{\text{CO}}$  values are consistent with, or even lower than, the predicted metallicity dependence, and, as at 250 pc, there is large scatter.

The large scatter and inconsistencies between the two data sets at different resolutions could also point to a dependence on additional parameters beyond metallicity. In particular, the comparison between Figs. 7 and 11 shows that the larger ACA beam, rebinned here to  $\sim 250$  pc, does not sample the brighter CO emission that emerges, instead, at  $\sim 40$  pc with the 12-m array. In the larger beam, there are more CO-faint regions than bright regions; consequently,  $X_{\text{CO}}$  is larger.

Trends of the  $\text{H}_2$  conversion factor  $X_{\text{CO}}$  with the observed CO velocity-integrated brightness temperature  $I_{\text{CO}}$  are also expected theoretically. Measured  $I_{\text{CO}}$  is mainly governed by mean density along the line-of-sight (e.g., Gong et al. 2018), since CO forms at higher volume densities ( $n \gtrsim 100\text{--}200 \text{ cm}^{-3}$ ) than  $\text{H}_2$  ( $n \sim 10\text{--}100 \text{ cm}^{-3}$ ). This implies that, for environments with similar metallicities,  $I_{\text{CO}}$  can be taken as a proxy of column or volume densities (e.g., Hu et al. 2022), and related to  $X_{\text{CO}}$ , either inferred from simulations, or measured empirically, as we have done here. It is likely that the underlying reason why at 40 pc the fainter regions have larger  $X_{\text{CO}}$  stems from the radiative transfer of CO; the faint CO emission regions are heavily subthermally excited and may even become optically thin due to the low volume and column densities with which they are associated. Subthermal excitation would make them less luminous in the CO line per hydrogen atom, compared to the higher density/column density gas with excitation temperatures approaching kinetic temperatures (e.g., Hu et al. 2022).

We have tested this hypothesis by plotting in Fig. 13  $X_{\text{CO}}$  inferred above at the two different resolutions against  $I_{\text{CO}}$  of the relevant data sets. An anticorrelation of  $X_{\text{CO}}$  with  $I_{\text{CO}}$  emerges

clearly from both sets of data, with Pearson correlation coefficients of  $-0.65$  (250 pc) and  $-0.7$  (40 pc). This correlation is almost certainly causing at least part of the scatter in our  $X_{\text{CO}}$  estimates shown in Figs. 8 and 12. We have performed a robust fit in logarithmic space to  $X_{\text{CO}}$  with  $I_{\text{CO}}$  shown as a yellow regression line in Fig. 13:

$$\log_{10} X_{\text{CO}} = \begin{cases} (-0.51 \pm 0.12) \log_{10} I_{\text{CO}} + (1.64 \pm 0.15) & 250 \text{ pc}, \tau_{160} \\ (-0.74 \pm 0.05) \log_{10} I_{\text{CO}} + (1.31 \pm 0.03) & 40 \text{ pc}, A_V \\ (-0.70 \pm 0.05) \log_{10} I_{\text{CO}} + (1.30 \pm 0.03) & 40 \text{ pc}, \tau_V. \end{cases} \quad (18)$$

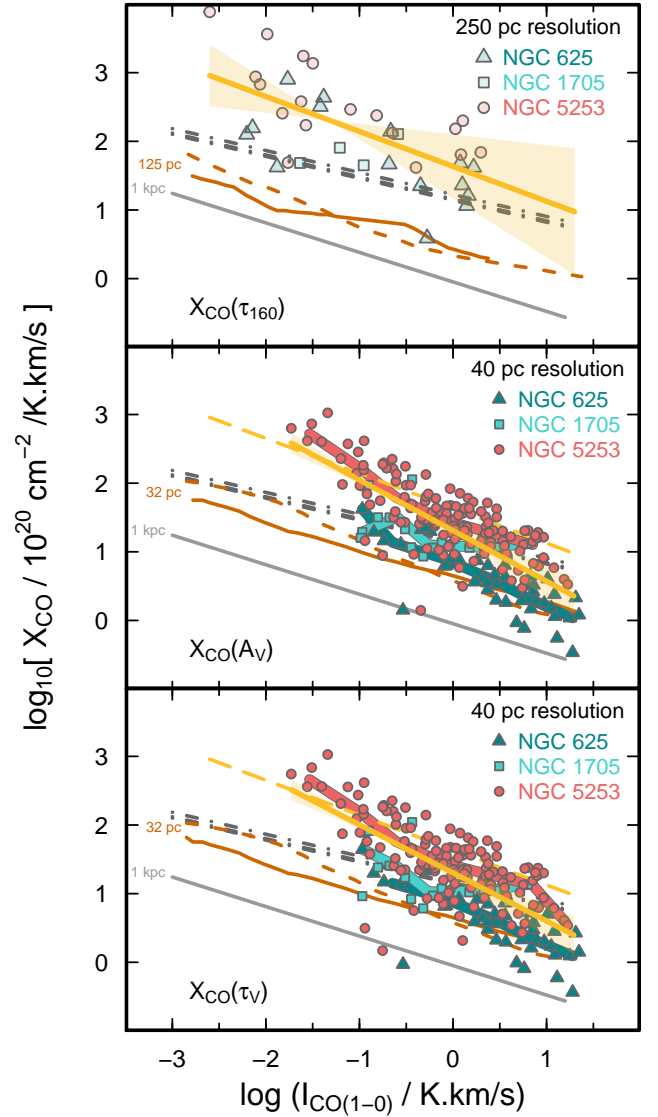
The best-fit parameters for  $X_{\text{CO}}$  estimated from the trends with  $A_V$  and  $\tau_V$  are similar, and also show a comparable mean dispersion. The slope and intercept of the 250 pc resolution data differ (at a  $\sim 2\sigma$  level) from those of the 40 pc fits, with the larger resolution data having flatter slope and a larger intercept. We expect these relations to be accurate for galaxies of around this metallicity,  $\sim \frac{1}{3} Z_{\odot}$ , but for higher and lower abundances, and different resolutions, more data are needed to establish similar empirical relations.

Narayanan et al. (2012) examined the dependence of  $X_{\text{CO}}$  on metallicities, gas temperatures, and velocity dispersion of the clouds. Using post-processing of the simulated galaxies by Narayanan et al. (2011) to determine the physical and chemical state of the molecular gas, Narayanan et al. (2012) also find that  $X_{\text{CO}}$  is well correlated with  $I_{\text{CO}}$ , and is a function of physical conditions within the clouds. They find a simple power-law dependence of  $X_{\text{CO}}$  on  $I_{\text{CO}}$  and metallicity (shown as dot-dashed lines in Fig. 13), with an  $I_{\text{CO}}$  power-law index (slope) of  $-0.32$ . Our observations are inconsistent with this slope, as it is significantly lower than the power-law index of  $-0.7$  (40 pc) found in our data (Eq. (18)); the  $-0.5$  slope of the 250 pc data is somewhat more consistent with the Narayanan et al. result, although still  $\gtrsim 2\sigma$  steeper.

To study CO emission at pc-scale resolutions, and measure  $X_{\text{CO}}$ , Gong et al. (2018, 2020) conducted solar-metallicity magneto-hydrodynamic galactic disk simulations with post-processing that includes a chemical network and radiative transfer. Their analysis finds a slight anticorrelation between  $X_{\text{CO}}$  and  $I_{\text{CO}}$ , but with a very shallow power-law slope of  $-0.011 \pm 0.005$ . Such a shallow slope is comparable to that of  $-0.05$  found empirically by Remy et al. (2017) for clouds in the MW anti-center, but much flatter than the well-defined dependence for our low-metallicity starbursts.

Recent work by Hu et al. (2022), based on hydrodynamical simulations, chemistry, and radiative transfer, predict that  $X_{\text{CO}}$  depends not only on metallicity but also on the spatial resolution of the maps and on the intensity of the emission line  $I_{\text{CO}}$ . In Fig. 13, we have reproduced their 32 pc and 125 pc curves for  $Z_{\odot}$  (dashed curves) and  $0.3 Z_{\odot}$  (solid ones) and their kpc-resolution trend that is valid for all metallicities. Our best-fit power-law slope of  $\sim -0.5$  for 250 pc resolution is not far from their value of  $-0.43$  (valid at 1 kpc for roughly all metallicities). At higher resolution, the individual trends found by Hu et al. (2022) for solar and  $0.3 Z_{\odot}$  metallicities with region sizes from 32 pc to 125 pc (shown by brown curves in Fig. 13) show similar slopes, somewhat shallower than what we measure. Nevertheless, the agreement between our observations and the predictions of Hu et al. (2022) is reasonably good especially at high  $I_{\text{CO}}$ .

Because of the expectation of more CO-dark gas in larger beams and at low metallicity, it is somewhat surprising that



**Fig. 13.**  $X_{\text{CO}}$  estimated from Eq. (8) versus  $I_{\text{CO}}$  in the top panel (250 pc resolution);  $X_{\text{CO}}$  from Eq. (14) in the middle (40 pc resolution); and from Eq. (15) in the lower (40 pc resolution). Also shown as dark-gray dot-dashed lines are the predictions from Narayanan et al. (2012) for the different metallicities of our targets. The 1 kpc trend from Hu et al. (2022), valid for all metallicities, is shown as a light-gray solid line (labeled “1 kpc”). The brown solid (dashed) curves correspond to  $0.3 Z_{\odot}$  ( $Z_{\odot}$ ) metallicities at 125 pc resolution (top panel) and at 32 pc (middle and lower ones). The  $0.3 Z_{\odot}$  curves are the best approximation to the metallicities of our target starbursts. The robust fit in logarithmic space to our data is shown as a dark-yellow line with  $1\sigma$  excursions by the yellow shaded area; in the lower panels, the dashed dark-yellow line reproduces the 250 pc best fit shown in the upper panel. The trends seen in our data follows the predictions of Hu et al. (2022), in terms of excursion, but we find a steeper slope and an overall higher normalization. We attribute this to the theoretical  $W_{10}$  not being the exact same quantity as observed  $I_{\text{CO}}$ , so we approximate  $W_{10}$  as  $I_{\text{CO}}$ , which is a better approximation at high  $I_{\text{CO}}$ , when  $X_{\text{CO}}$  is low, but which is far from true at low  $I_{\text{CO}}$ , when  $X_{\text{CO}}$  is high. See text for more details.

the Hu et al. simulations find that  $X_{\text{CO}}$  is smaller with increasing beam size and decreasing metallicity. This can be understood because of the distinction between the theoretical  $W_{10}$  in Hu et al. (2022) and the observed quantity  $I_{\text{CO}}$ . The cosmic microwave background (CMB) temperature,  $T_{\text{BG}}$ , must be



subtracted to calibrate observed antenna temperature,  $I_{\text{CO}}$ ; thus  $I_{\text{CO}}$  will be identically 0 for excitation temperature  $T_{\text{ex}} = 2.73$  K, while  $W_{10}$  is only zero when  $N_{\text{CO}}$  is zero, whatever  $T_{\text{ex}}$ . This implies that their CO-dark gas radiates even at low  $\text{H}_2$  density, but in the observed signal  $I_{\text{CO}}$ , it does not. Their conclusion therefore is expected to underestimate the amount of CO-dark gas.

The results of [Hu et al. \(2022\)](#) suggest that observed velocity-integrated  $T_{\text{B}}$  below  $\sim 10 \text{ K km s}^{-1}$  are optically thin, and thus directly trace CO column density  $N_{\text{CO}}$  (for  $N_{\text{CO}} \lesssim 10^{16} \text{ cm}^{-2}$ ). This would imply that virtually all our observations are optically thin since there are very few resolution elements brighter than this limit. Most of the variation of  $X_{\text{CO}}$  is expected to occur in the optically thin regime, as it is regulated by CO abundance and its formation by the transition from atomic carbon. Our observations are apparently consistent with these expectations, since over a roughly 3 orders of magnitude change in  $I_{\text{CO}}$ ,  $X_{\text{CO}}$  also varies by a similar factor. Nevertheless, at the lowest  $I_{\text{CO}}$  (lowest column densities), at both the 250 pc and 40 pc resolutions  $X_{\text{CO}}$  exceeds by a factor of 10 or so the predictions of the [Hu et al.](#) simulations. Also, the difference we find between 250 pc and 40 pc resolution seems not to be a vertical shift, but rather a continuation to lower surface brightnesses as shown in [Fig. 13](#). Since our targets are all at roughly the same  $1/3 Z_{\odot}$  abundance, we are unable to test observational variation with metallicity. In any case, overall, our observations agree with [Hu et al. \(2022\)](#) that  $X_{\text{CO}}$  is a multi-variate function of three observables,  $I_{\text{CO}}$ , metallicity, and beam size.

## 7. Discussion and conclusions

Perhaps the most significant caveat in our methodology is the assumption of a single DGR across each of the galaxies, independently of spatial scale. Rigorously speaking,  $X_{\text{CO}}$  and the DGR should be measured independently within each spatial element, as done by [Sandstrom et al. \(2013\)](#) on  $\sim \text{kpc}$  scales. In the study of the SMC by [Bolatto et al. \(2011\)](#), on  $\sim 200$  pc scales, the DGR varies by  $\sim 0.4$  dex along the SMC Bar, the Wing, and within the star-forming regions N83/N84. The assumption of a constant DGR is intimately related to our estimate of  $X_{\text{CO}}$ , at least where CO emission dominates over HI. If we assume a constant metallicity-dependent value for  $X_{\text{CO}}$ , as shown in the right panel of [Fig. 8](#), we infer decreasing DGRs toward higher dust column densities. This effect may be real, but for our targets, with relatively few 250 pc resolution elements, it is impossible to assess spatial variations in the DGR, and disentangle them from variations in  $X_{\text{CO}}$ .

### 7.1. Additional considerations

Putting this caveat aside, our analysis ([Figs. 8 and 12](#)) suggests that  $X_{\text{CO}}$  is not correlated with either dust optical depth ( $\tau_{160}$ ) or visual extinction/optical depth ( $A_V$ ,  $\tau_V$ ). This would be in disagreement with the individual cloud models by [Glover & Mac Low \(2011\)](#) and [Shetty et al. \(2011\)](#) who find a threshold effect for  $A_V \lesssim 1$  mag. However, our observations do not resolve individual clouds, so that the discrepancy could be simply a question of spatial resolution. As pointed out by [Gong et al. \(2018\)](#), a resolution of  $\lesssim 2$  pc is necessary to resolve the average  $X_{\text{CO}}$  within molecular clouds for conditions similar to the solar neighborhood; at lower metallicity, given the small  $\sim \text{pc}$  scales, possibly even better resolution would be required.

Various recent simulations find that  $X_{\text{CO}}$  is related to  $I_{\text{CO}}$  and also to spatial scale, that is to say the region over which the

parameters are averaged (e.g., [Gong et al. 2018, 2020; Hu et al. 2022](#)); observationally, spatial scale corresponds to beam size, or in our case the scale imposed by rebinning. We would argue that these parameters,  $I_{\text{CO}}$  and spatial scale, are partially dependent, as shown in [Fig. 13](#); relative to the 40 pc data, the data at 250 pc extend to fainter CO emission, but do not reach the brighter CO emission. It is very difficult to achieve high values of  $I_{\text{CO}}$  with large beams as can also be appreciated by the comparison of [Figs. 7 and 11](#).

Moreover, as might be intuitively expected, the fraction of CO-faint or dark gas is expected to increase with increasing beam size ([Gong et al. 2018; Hu et al. 2022](#)). Part of this depends on the  $I_{\text{CO}}$  lower limit (imposed on the simulations, or observationally by signal-to-noise), and part is due to the erosion of the CO-emitting volumes by photodissociation. Photodissociation results in regions that are dominated by carbon in atomic or ionized phases, CI and CII, rather than CO, and these regions can be much more extended than the CO emission.

### 7.2. Summary

We have derived  $X_{\text{CO}}$  in three low-metallicity starbursts, NGC 625, NGC 1705, and NGC 5253, using ALMA 12-m data at  $\sim 40$  pc resolution and ACA observations at  $\sim 250$  pc resolution, together with a dust-based method to infer  $N_{\text{H}_2}$ . Our work can be summarized as follows:

- We fit the flux in *Herschel* PACS maps to two-temperature MBBs in order to quantify dust optical depth  $\tau_{160}$ , and compare it with HI maps and CO maps measured with ACA, all rebinned to  $\sim 250$  pc resolution.
- By approximating the trends of HI and CO versus  $\tau_{160}$  with linear functions and ones that reflect radiative transfer, we have quantified the DGR for each galaxy and the level at which HI is converted to  $\text{H}_2$ . This makes it possible to estimate  $X_{\text{CO}}$  at 250 pc resolution and compare it to what would be expected from global metallicity estimates for  $X_{\text{CO}}$ . We find that the  $X_{\text{CO}}$  values at 250 pc resolution can be as much as an order of magnitude larger than what would be expected from metallicity trends. There is also large scatter implying, possibly, spatial variation of  $X_{\text{CO}}$  at this resolution.
- At  $\sim 40$  pc resolution, roughly the native 12-m ALMA beam, we compare CO measured with the ALMA 12-m array and  $A_V$ , estimated from the VLT/MUSE maps of the Balmer decrement. We eschew the assumption of  $A_V$  as a foreground screen, and instead infer  $\tau_V$  from  $A_V$  by assuming that the extinguishing dust is well mixed with the ionized gas. Overall, this turns out to be the better assumption, as supported by the closer agreement of our data with the Galactic GMCs (see [Fig. 11](#)). By fitting the CO versus  $A_V$  or  $\tau_V$  trends, we have been able to identify in our data an  $A_V$  threshold for CO emission of  $\sim 0.1$  mag for all three galaxies. This is significantly smaller than the  $\sim 1$  mag  $A_V$  threshold found in simulations (e.g., [Glover & Clark 2016](#)) or observations of MW molecular clouds (e.g., [Pineda et al. 2008](#)).
- Incorporating the DGR measured at 250 pc resolution, and the  $A_V$  transition from HI to  $\text{H}_2$  at high dust optical depths  $A_V^{\text{Hcrit}}$ , we are able to infer  $X_{\text{CO}}$  on 40 pc scales. Results are generally consistent with the expectations from a global metallicity-dependence of  $X_{\text{CO}}$ , except for NGC 625 which shows values typically encountered in environments closer to solar metallicity. This almost certainly stems from the higher  $A_V^{\text{Hcrit}}$  found for this galaxy ( $\sim 0.9$  mag relative to  $\sim 0.2$ – $0.3$  mag), and when we estimate  $X_{\text{CO}}$  using these lower

values also for NGC 625,  $X_{\text{CO}}$  becomes consistent with metallicity expectations. As for the 250 pc  $X_{\text{CO}}$  analysis, there is large scatter.

- Finally, we compare  $X_{\text{CO}}$  to CO brightness temperature  $I_{\text{CO}}$ , predicted by simulations to be closely related. Figure 13 shows that the two quantities are highly anticorrelated, with power-law slopes steeper than those found by the simulations of Narayanan et al. (2012) and Gong et al. (2018), although possibly consistent with the slope of  $\sim -0.4$  found by Hu et al. (2022) across a range of resolutions. Relative to Narayanan et al. (2012) and Hu et al. (2022), because of the difference in power-slopes between the data and the simulations, the data show a higher normalization of the relation between  $X_{\text{CO}}$  and  $I_{\text{CO}}$  for faint CO emission levels. Despite these differences in details, our observations confirm that  $X_{\text{CO}}$  depends not only on metallicity, but, also on beam size, and CO surface brightness  $I_{\text{CO}}$ . Such behavior can be attributed to the increasing fraction of CO-dark  $\text{H}_2$  gas with lower spatial resolution (larger beams) and lower surface-brightness emission.

Our analysis is limited to three low-metallicity starbursts all of the same metallicity,  $\sim 0.3 Z_{\odot}$ . Thus, we are sampling only a narrow range of subsolar metal abundance. Future work would profit from a broader spread in metallicities and spatial resolution, and inclusion of metal-poor dwarf galaxies that are forming stars more quiescently than the starbursts studied here.

*Acknowledgements.* We would like to thank the referee for thoughtful, constructive comments that greatly improved the paper. This paper makes use of the following ALMA data: ADS/JAO.ALMA#2018.1.00219.S. ALMA is a partnership of ESO (representing its member states), NSF (USA), and NINS (Japan), together with NRC (Canada), MOST, and ASIAA (Taiwan), and KASI (Republic of Korea), in cooperation with the Republic of Chile. The Joint ALMA Observatory is operated by ESO, AUI/NRAO and NAOJ. This work was partly done using GNU Astronomy Utilities (Gnuastro, [ascl1.net/1801.009](https://github.com/wkward/gnuastro)) version 0.15. Work on Gnuastro has been funded by the Japanese Ministry of Education, Culture, Sports, Science, and Technology (MEXT) scholarship and its Grant-in-Aid for Scientific Research (21244012, 24253003), the European Research Council (ERC) advanced grant 339659-MUSICOS, European Union’s Horizon 2020 research and innovation programme under Marie Skłodowska-Curie grant agreement No 721463 to the SUNDIAL ITN, and from the Spanish Ministry of Economy and Competitiveness (MINECO) under grant number AYA2016-76219-P. SGB acknowledges support from the research project PID2019-106027GA-C44 of the Spanish Ministerio de Ciencia e Innovación, and GV acknowledges support from ANID program FONDECYT Postdoctorado 3200802.

## References

Accurso, G., Saintonge, A., Catinella, B., et al. 2017, *MNRAS*, 470, 4750  
 Akhlaghi, M. 2018, Astrophysics Source Code Library [record ascl:1801.009]  
 Altintas, I., Barney, O., Cheng, Z., et al. 2006, *J. Phys. Conf. Ser.*, 46, 468  
 Aniano, G., Draine, B. T., Gordon, K. D., & Sandstrom, K. 2011, *PASP*, 123, 1218  
 Annibali, F., Tosi, M., Monelli, M., et al. 2009, *AJ*, 138, 169  
 Annibali, F., Tosi, M., Pasquali, A., et al. 2015, *AJ*, 150, 143  
 Bell, T. A., Roueff, E., Viti, S., & Williams, D. A. 2006, *MNRAS*, 371, 1865  
 Berg, D. A., Skillman, E. D., Marble, A. R., et al. 2012, *ApJ*, 754, 98  
 Bigiel, F., Leroy, A., Walter, F., et al. 2008, *AJ*, 136, 2846  
 Billett, O. H., Hunter, D. A., & Elmegreen, B. G. 2002, *AJ*, 123, 1454  
 Bisbas, T. G., Tan, J. C., & Tanaka, K. E. I. 2021, *MNRAS*, 502, 2701  
 Bohlin, R. C., Savage, B. D., & Drake, J. F. 1978, *ApJ*, 224, 132  
 Bolatto, A. D., Jackson, J. M., & Ingalls, J. G. 1999, *ApJ*, 513, 275  
 Bolatto, A. D., Leroy, A. K., Rosolowsky, E., Walter, F., & Blitz, L. 2008, *ApJ*, 686, 948  
 Bolatto, A. D., Leroy, A. K., Jameson, K., et al. 2011, *ApJ*, 741, 12  
 Bolatto, A. D., Wolfire, M., & Leroy, A. K. 2013, *ARA&A*, 51, 207  
 Boquien, M., Boselli, A., Buat, V., et al. 2013, *A&A*, 554, A14  
 Calzetti, D., Meurer, G. R., Bohlin, R. C., et al. 1997, *AJ*, 114, 1834  
 Calzetti, D., Johnson, K. E., Adamo, A., et al. 2015, *ApJ*, 811, 75  
 Cannon, J. M., Dohm-Palmer, R. C., Skillman, E. D., et al. 2003, *AJ*, 126, 2806

Cannon, J. M., McClure-Griffiths, N. M., Skillman, E. D., & Côté, S. 2004, *ApJ*, 607, 274  
 Cannon, J. M., Skillman, E. D., Sembach, K. R., & Bomans, D. J. 2005, *ApJ*, 618, 247  
 Cannon, J. M., Smith, J.-D. T., Walter, F., et al. 2006, *ApJ*, 647, 293  
 Cardelli, J. A., Clayton, G. C., & Mathis, J. S. 1989, *ApJ*, 345, 245  
 Casasola, V., Bianchi, S., Magrini, L., et al. 2022, *A&A*, 668, A130  
 Cignoni, M., Sacchi, E., Aloisi, A., et al. 2018, *ApJ*, 856, 62  
 Cignoni, M., Sacchi, E., Tosi, M., et al. 2019, *ApJ*, 887, 112  
 Cormier, D., Madden, S. C., Lebouteiller, V., et al. 2014, *A&A*, 564, A121  
 Côté, S., Carignan, C., & Freeman, K. C. 2000, *AJ*, 120, 3027  
 Cresci, G., Vanzi, L., & Sauvage, M. 2005, *A&A*, 433, 447  
 Croxall, K. V., van Zee, L., Lee, H., et al. 2009, *ApJ*, 705, 723  
 Di Teodoro, E. M., & Fraternali, F. 2015, *MNRAS*, 451, 3021  
 Disney, M., Davies, J., & Phillipps, S. 1989, *MNRAS*, 239, 939  
 Draine, B. T. 1978, *ApJS*, 36, 595  
 Draine, B. T. 2003, *ApJ*, 598, 1017  
 Elson, E. C., de Blok, W. J. G., & Kraan-Korteweg, R. C. 2013, *MNRAS*, 429, 2550  
 Emsellem, E., Schinnerer, E., Santoro, F., et al. 2022, *A&A*, 659, A191  
 Feldmann, R., Gnedin, N. Y., & Kravtsov, A. V. 2012, *ApJ*, 747, 124  
 Freudling, W., Romaniello, M., Bramich, D. M., et al. 2013, *A&A*, 559, A96  
 Galametz, M., Kennicutt, R. C., Albrecht, M., et al. 2012, *MNRAS*, 425, 763  
 Glover, S. C. O., & Clark, P. C. 2016, *MNRAS*, 456, 3596  
 Glover, S. C. O., & Mac Low, M. M. 2011, *MNRAS*, 412, 337  
 Gong, M., Ostriker, E. C., & Wolfire, M. G. 2017, *ApJ*, 843, 38  
 Gong, M., Ostriker, E. C., & Kim, C.-G. 2018, *ApJ*, 858, 16  
 Gong, M., Ostriker, E. C., Kim, C.-G., & Kim, J.-G. 2020, *ApJ*, 903, 142  
 Heckman, T. M., Sembach, K. R., Meurer, G. R., et al. 2001, *ApJ*, 554, 1021  
 Hensley, B. S., & Draine, B. T. 2021, *ApJ*, 906, 73  
 Hollenbach, D. J., & Tielens, A. G. G. M. 1997, *ARA&A*, 35, 179  
 Hu, C.-Y., Schrubba, A., Sternberg, A., & van Dishoeck, E. F. 2022, *ApJ*, 931, 28  
 Hughes, T. M., Baes, M., Fritz, J., et al. 2014, *A&A*, 565, A4  
 Hunt, L. K., Draine, B. T., Bianchi, S., et al. 2015, *A&A*, 576, A33  
 Hunt, L. K., Weiß, A., Henkel, C., et al. 2017, *A&A*, 606, A99  
 Hunt, L. K., Tortora, C., Ginolfi, M., & Schneider, R. 2020, *A&A*, 643, A180  
 Imapara, N., De Looze, I., Faesi, C. M., & Cormier, D. 2020, *ApJ*, 895, 21  
 Indebetouw, R., Brogan, C., Chen, C. H. R., et al. 2013, *ApJ*, 774, 73  
 Karachentsev, I. D., Makarov, D. I., & Kaisina, E. I. 2013, *AJ*, 145, 101  
 Kirkpatrick, A., Calzetti, D., Kennicutt, R., et al. 2014, *ApJ*, 789, 130  
 Kobulnicky, H. A., & Skillman, E. D. 2008, *AJ*, 135, 527  
 Kobulnicky, H. A., Skillman, E. D., Roy, J.-R., Walsh, J. R., & Rosa, M. R. 1997, *ApJ*, 477, 679  
 Krumholz, M. R., McKee, C. F., & Tumlinson, J. 2009, *ApJ*, 693, 216  
 Lee, C., Leroy, A. K., Schnee, S., et al. 2015, *MNRAS*, 450, 2708  
 Lee, C., Leroy, A. K., Bolatto, A. D., et al. 2018, *MNRAS*, 474, 4672  
 Lelli, F., Verheijen, M., & Fraternali, F. 2014a, *A&A*, 566, A71  
 Lelli, F., Verheijen, M., & Fraternali, F. 2014b, *MNRAS*, 445, 1694  
 Leroy, A. K., Bolatto, A., Bot, C., et al. 2009, *ApJ*, 702, 352  
 Leroy, A. K., Lee, C., Schrubba, A., et al. 2013, *ApJ*, 769, L12  
 Lombardi, M., Alves, J., & Lada, C. J. 2006, *A&A*, 454, 781  
 López-Sánchez, Á. R., Koribalski, B. S., van Eymeren, J., et al. 2012, *MNRAS*, 419, 1051  
 Madden, S. C., Rémy-Ruyer, A., Galametz, M., et al. 2013, *PASP*, 125, 600  
 Marasco, A., Belfiore, F., Cresci, G., et al. 2023, *A&A*, 670, A92  
 Martins, F., Förster Schreiber, N. M., Eisenhauer, F., & Lutz, D. 2012, *A&A*, 547, A17  
 McMullin, J. P., Waters, B., Schiebel, D., Young, W., & Golap, K. 2007, *ASP Conf. Ser.*, 376, 127  
 McQuinn, K. B. W., Skillman, E. D., Cannon, J. M., et al. 2010, *ApJ*, 721, 297  
 Misselt, K. A., Gordon, K. D., Clayton, G. C., & Wolff, M. J. 2001, *ApJ*, 551, 277  
 Miura, R. E., Espada, D., Hirota, A., et al. 2018, *ApJ*, 864, 120  
 Monreal-Ibero, A., Walsh, J. R., Iglesias-Páramo, J., et al. 2017, *A&A*, 603, A130  
 Narayanan, D., Krumholz, M., Ostriker, E. C., & Hernquist, L. 2011, *MNRAS*, 418, 664  
 Narayanan, D., Krumholz, M. R., Ostriker, E. C., & Hernquist, L. 2012, *MNRAS*, 421, 3127  
 Natta, A., & Panagia, N. 1984, *ApJ*, 287, 228  
 O’Connell, R. W., Gallagher, J. S., & I., & Hunter, D. A., 1994, *ApJ*, 433, 65  
 O’Donnell, J. E. 1994, *ApJ*, 422, 158  
 Ott, S. 2010, *ASP Conf. Ser.*, 434, 139  
 Pak, S., Jaffe, D. T., van Dishoeck, E. F., Johansson, L. E. B., & Booth, R. S. 1998, *ApJ*, 498, 735  
 Papadopoulos, P. P., Thi, W. F., & Viti, S. 2004, *MNRAS*, 351, 147  
 Pilyugin, L. S., Grebel, E. K., & Zinchenko, I. A. 2015, *MNRAS*, 450, 3254  
 Pineda, J. E., Caselli, P., & Goodman, A. A. 2008, *ApJ*, 679, 481

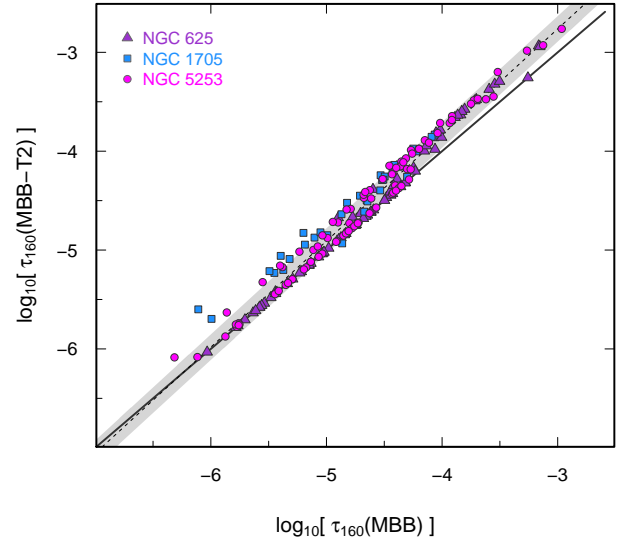
- Planck Collaboration XI. 2014, [A&A](#), **571**, A11
- Poglitich, A., Waelkens, C., Geis, N., et al. 2010, [A&A](#), **518**, L2
- Remy, Q., Grenier, I. A., Marshall, D. J., & Casandjian, J. M. 2017, [A&A](#), **601**, A78
- Rémy-Ruyer, A., Madden, S. C., Galliano, F., et al. 2014, [A&A](#), **563**, A31
- Rubio, M., Lequeux, J., & Boulanger, F. 1993, [A&A](#), **271**, 9
- Rubio, M., Elmegreen, B. G., Hunter, D. A., et al. 2015, [Nature](#), **525**, 218
- Sabbi, E., Calzetti, D., Ubeda, L., et al. 2018, [ApJS](#), **235**, 23
- Sanders, D. B., Solomon, P. M., & Scoville, N. Z. 1984, [ApJ](#), **276**, 182
- Sandstrom, K. M., Leroy, A. K., Walter, F., et al. 2013, [ApJ](#), **777**, 5
- Schaerer, D., Contini, T., Kunth, D., & Meynet, G. 1997, [ApJ](#), **481**, L75
- Schruba, A., Leroy, A. K., Kruijssen, J. M. D., et al. 2017, [ApJ](#), **835**, 278
- Shetty, R., Glover, S. C., Dullemond, C. P., & Klessen, R. S. 2011, [MNRAS](#), **412**, 1686
- Shi, Y., Wang, J., Zhang, Z.-Y., et al. 2020, [ApJ](#), **892**, 147
- Skillman, E. D., Côté, S., & Miller, B. W. 2003a, [AJ](#), **125**, 593
- Skillman, E. D., Côté, S., & Miller, B. W. 2003b, [AJ](#), **125**, 610
- Sternberg, A., Le Petit, F., Roueff, E., & Le Bourlot, J. 2014, [ApJ](#), **790**, 10
- Tokuda, K., Kondo, H., Ohno, T., et al. 2021, [ApJ](#), **922**, 171
- Tosi, M., Sabbi, E., Bellazzini, M., et al. 2001, [AJ](#), **122**, 1271
- Turner, J. L., Beck, S. C., & Hurt, R. L. 1997, [ApJ](#), **474**, L11
- Turner, J. L., Beck, S. C., & Ho, P. T. P. 2000, [ApJ](#), **532**, L109
- Turner, J. L., Beck, S. C., Benford, D. J., et al. 2015, [Nature](#), **519**, 331
- Turner, J. L., Consiglio, S. M., Beck, S. C., et al. 2017, [ApJ](#), **846**, 73
- van Dishoeck, E. F., & Black, J. H. 1988, [ApJ](#), **334**, 771
- Vazdekis, A., Koleva, M., Ricciardelli, E., Röck, B., & Falcón-Barroso, J. 2016, [MNRAS](#), **463**, 3409
- Vázquez, G. A., Leitherer, C., Heckman, T. M., et al. 2004, [ApJ](#), **600**, 162
- Visser, R., van Dishoeck, E. F., & Black, J. H. 2009, [A&A](#), **503**, 323
- Weilbacher, P. M., Palsa, R., Streicher, O., et al. 2020, [A&A](#), **641**, A28
- Westmoquette, M. S., James, B., Monreal-Ibero, A., & Walsh, J. R. 2013, [A&A](#), **550**, A88
- Whelan, D. G., Johnson, K. E., Whitney, B. A., Indebetouw, R., & Wood, K. 2011, [ApJ](#), **729**, 111
- Wiklind, T., & Henkel, C. 1989, [A&A](#), **225**, 1
- Wilson, C. D., Rangwala, N., Glenn, J., et al. 2014, [ApJ](#), **789**, L36
- Witt, A. N., & Gordon, K. D. 1996, [ApJ](#), **463**, 681
- Witt, A. N., & Gordon, K. D. 2000, [ApJ](#), **528**, 799
- Wolfire, M. G., Hollenbach, D., & Tielens, A. G. G. M. 1993, [ApJ](#), **402**, 195
- Wolfire, M. G., Hollenbach, D., & McKee, C. F. 2010, [ApJ](#), **716**, 1191

## Appendix A: Details of the fits to the PACS data to derive $\tau_{160}$

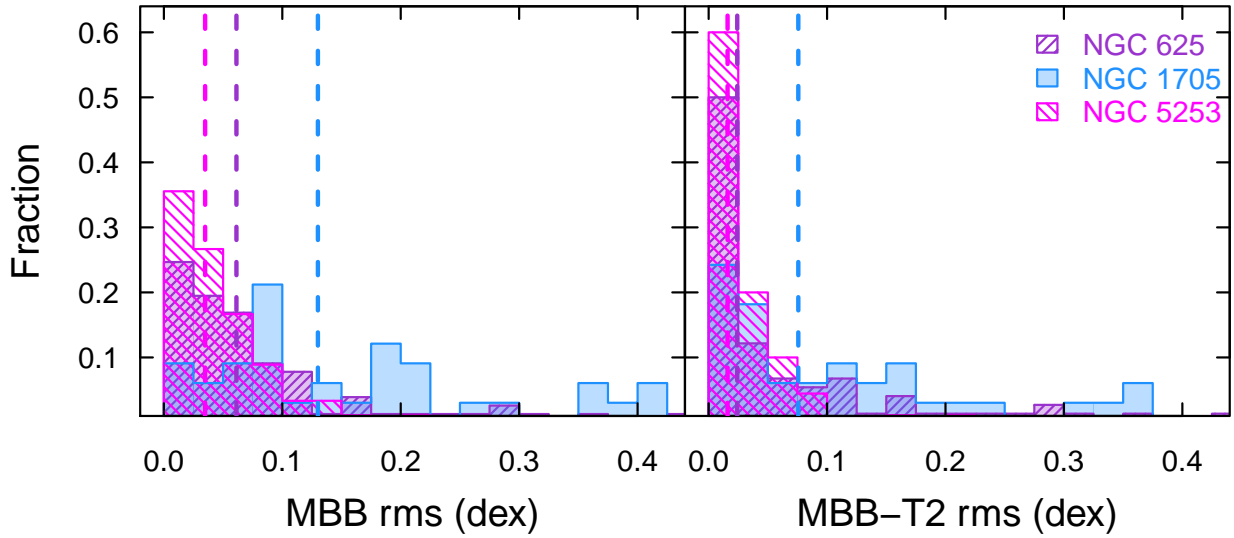
The  $160\ \mu\text{m}$  optical depths  $\tau_{160}$  of the two approaches (namely modified single-temperature blackbodies, MBB, and modified two-temperature blackbodies, MBB-2T) are compared in Fig. A.1. The scatter of the comparison (with imposed  $\gamma \geq 0$ ) is  $\sim 0.13$  dex, with  $\tau_{160}(\text{MBB-T2})$  larger than  $\tau_{160}(\text{MBB})$ , as shown by the nonunit power-law slope and positive intercept of the best (robust) fit.

The distributions of the rms (calculated as the root-mean-square difference in  $\log_{10}$  space between the model and the data) of the two fits are reported in Fig. A.2. Given that the expected uncertainty in the individual PACS photometry is  $\sim 10\%$ , the rms values of both MBB and MBB-T2 fits are quite good, and, except for NGC 1705, well within the expected error. However, the MBB-T2 fits are overall superior to MBB, possibly due to the extra fitted parameter and the consequent zero degrees of freedom. Three regions in both NGC 625 and NGC 5253 are not included in Fig. A.2, because of  $\text{rms} > 0.5$  due to the very low  $70\ \mu\text{m}$  fluxes and the consequent poor fits.

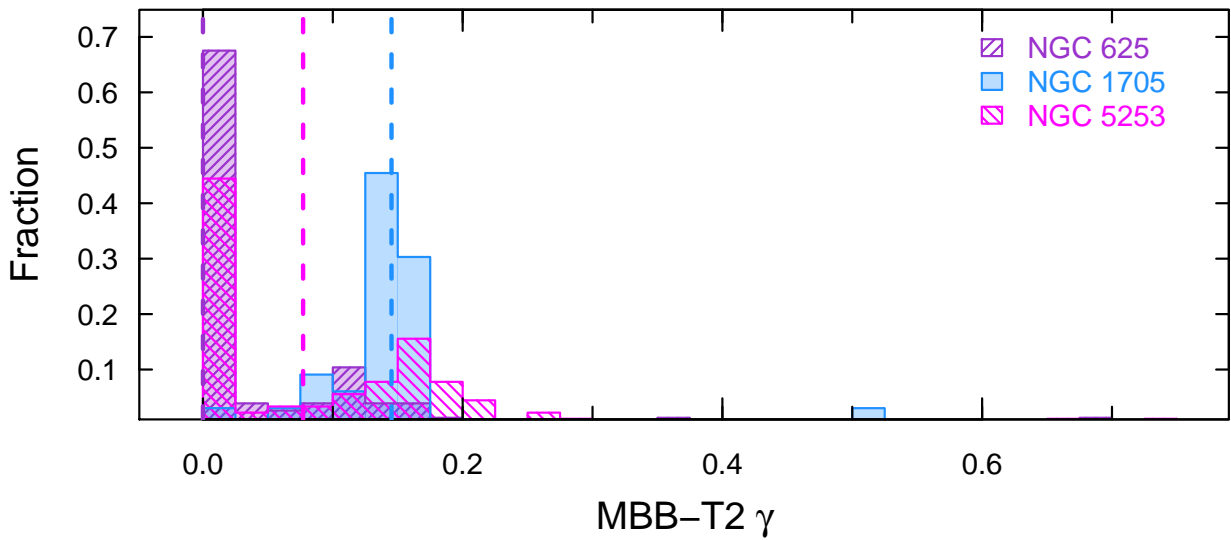
The overall  $\gamma$  distribution (restricted to  $0 \leq \gamma \leq 1$ ) is shown in Fig. A.3. There are (45, 0, 33) fits for NGC (625, 1705, 5253), respectively, that would have preferred either  $\gamma < 0$  (58%, 0, 37%). The median  $\gamma = 0.0$  for NGC 625 is associated with the relatively high fraction ( $45/77 = 58\%$ ) of regions that would have been best fit with these anomalous  $\gamma$  values.



**Fig. A.1.**  $\tau_{160}$  from MBB-T2 fits plotted against MBB  $\tau_{160}$ .  $\log \tau_{160}(\text{MBB-T2}) = (1.073 \pm 0.010) \log \tau_{160}(\text{MBB}) + (0.46 \pm 0.05)$ . The scatter of the comparison is  $\sim 0.13$  dex; the shaded region denotes  $\pm 1\sigma$  relative to the best fit. In general,  $\tau_{160}(\text{MBB-T2})$  is larger than  $\tau_{160}(\text{MBB})$ , as shown by the nonunit power-law slope and positive intercept.



**Fig. A.2.** Distributions of rms values from MBB (left) and MBB-T2 (right) fits. Median values for each galaxy are shown by vertical dashed lines. The rms values of the MBB-T2 fits is generally excellent, possibly due to the extra fitted parameter and the consequent zero degrees of freedom. There are 3 regions each in NGC 625 and NGC 5253 not included here because their rms values exceeded 0.5 dex.



**Fig. A.3.** Distribution of fitted  $\gamma$  from MBB-T2 fits. The vertical dashed lines show the median fraction of IR emission due to the warmer component: (0.00, 0.14, 0.08) for NGC (625, 1705, 5253).